Experimental Investigation on Evaporation Induced Convection in Water Using Laser Based Measurement Techniques

University of Alberta

Experimental Investigation on Evaporation Induced Convection in Water Using Laser Based Measurement Techniques

by

Xudong Song

A thesis submitted to the Faculty of Graduate Studies and Research in partial fulfillment of the requirements for the degree of

Master of Science

Department of Mechanical Engineering

Examining Committee

David S. Nobes (Supervisor), Mechanical Engineering

Larry W. Kostiuk, Mechanical Engineering

Janet A.W. Elliott, Chemical and Materials Engineering

ABSTRACT

Recent studies showed that evaporation of water can induce surface tension gradients along the water surface and ultimately lead to convection, known as Marangoni convection. This study was devoted to visualization and characterization of the evaporation-induced, surface-tension-driven convection in water using laser-based measurement techniques.

The evaporation of water at various low vapor-phase pressures in the absence of buoyancy driven flow was investigated. Strong symmetric convection was observed and its velocity field was measured using stereo particle image velocimetry. The temperature field obtained from using both a thermocouple and planar laser induced fluorescence indicated that no buoyancy driven flow was generated. The strength of the convection was found to be correlated with the evaporation rate of water. In addition, the estimated Marangoni number exceeded the critical value for onset of Marangoni convection. It can be concluded that the observed evaporative convection of water can only be Marangoni convection.

ACKNOWLEDGEMENT

I would like to express my deeply appreciation to my supervisor, Dr. David Nobes, whose expert advice has guided me through this research journey and my writing of this thesis. The skills I've learned from him are invaluable and will last for lifetime. I would also like to thank my previous supervisor, Dr. Payam Rahimi, who has defined this project and explained it to me with patience. He also gave me comments on research even after leaving.

TABLE OF CONTENTS

LIST OF TABLES

LIST OF FIGURES

NOMENCLATURE

Abbreviations

2-D	two dimensional
3-D	three dimensional
CCD	charge-coupled device
FOV	field of view
LIF	laser induced fluorescence
Ma	Marangoni number
M^2	beam quality factor
PLIF	planar laser induced fluorescence
RhB	rhodamine B
Rh110	rhodamine 110
stereo-PIV	stereo particle image velocimetry
TC	thermocouple
TEC	thermoelectric cooling device

Symbols

C	dye concentration
D	liquid layer thickness
I_0	laser intensity
I_f	fluorescence intensity
Q	quantum efficiency
t	time
T	temperature
x	horizontal axis
y	vertical axis
$\partial T / \partial D$	temperature gradient
α	thermal diffusivity
γ	surface tension
η	dynamic viscosity
ε	molar absorptivity

Subscripts

LV	liquid-vapor interface
B	bottom
L	liquid

CHAPTER 1 : INTRODUCTION

The study of Marangoni convection in pure water has been limited and needs to be developed [1]. The objective of this study was to investigate evaporation induced convection in water in the absence of buoyancy driven flow. To characterize the convection and determine its driving mechanism, the velocity and temperature field in the bulk water needed to be measured. Therefore, stereo particle image velocimetry (stereo-PIV) and planar laser induced fluorescence (PLIF or planar LIF) were applied for velocity and temperature measurement respectively.

1.1 Marangoni convection

An important property of a liquid surface is surface tension which is caused by attraction among the liquid's molecules by intermolecular forces [2]. Variation of temperature, concentration or electric potential along the liquid surface can result in surface tension gradients which could induce a fluid motion known as Marangoni (or thermocapillary, or surface tension driven) convection [3]. The surface tension gradients drive liquid from low surface tension regions to high surface tension regions along the liquid surface. Marangoni convection is known as a key parameter in many engineering applications, including heat-mass transfer, surface coating, and production of materials [4].

Marangoni convection had been first proposed by Carlo Marangoni [5], who studied the effects of one liquid spreading upon another. He proved that for two given liquids, if the sum of the interfacial tension and the surface tension of one of the liquids is lower than the surface tension of the other one, the former liquid spreads on the latter one. A typical phenomenon of Marangoni convection is 'Tears of wine' which is induced by surface tension gradient as a result of concentration difference along the surface. It was first correctly explained by James Thomson [6, 7], who found out that flows would be generated if there were non-uniform concentration induced surface tension gradients along the surface of a liquid. He also distinguished surface tension-driven flow from buoyancy driven flow. At the beginning of the twentieth century, Benard [8, 9] observed cellular convective motion in thin liquid layers heated from below. The observed motion was attributed to Rayleigh convection until half a century later, Pearson [10] showed that it could also be produced by surface tension.

In order to determine how the surface tension may affect the stability of the liquid layers, Pearson [10] performed a small disturbance analysis for the theoretical case of an infinite homogeneous thin liquid layer of uniform thickness. The liquid layer has a free upper surface and lower surface in contact with a fixed plane. The only physical quantities that were assumed to vary within the liquid are temperature and parameters that were considered to depend on temperature only, i.e., surface tension and the rate of heat loss from the surface. The temperature in the liquid layer was assumed to decrease from the bottom to the surface linearly. Pearson indicated that onset of the surface tension driven convection is determined by a dimensionless number, the Marangoni number (*Ma*), i.e., the ratio of surface tension to viscous forces. It can be expressed as:

$$Ma = \left(-\frac{\partial \gamma}{\partial T} \right) \left(\frac{\partial T}{\partial D} \right) \frac{D^2}{\eta \alpha} \tag{1-1}$$

where, γ is the surface tension; T, local temperature of the liquid; D, the liquid layer thickness (characteristic length); $\partial T / \partial D$, the temperature gradient in the liquid; η, the dynamic viscosity; and α, represents the thermal diffusivity. While evaporation was ignored, Pearson found that Marangoni convection exists only when *Ma* exceeds a threshold value, 80. Some studies [11, 12] have experimentally examined the critical value of *Ma*. The results were found to be substantially close to the theoretical value proposed by Pearson.

The study of Marangoni convection has been well investigated for many liquids other than water [1]. Previous studies [13-18] have shown that evaporation of a liquid with a free surface could produce surface temperature gradients which would lead to interfacial instabilities and ultimately result in convections in the liquid. However, for water, Marangoni convection is usually weak and can be barely observed in typical experiments [19-23].

Some studies [19-23] stated that no Marangoni convection was observed in pure water even when *Ma* was greater than the threshold value, 80. In these investigations, the temperature profile in the evaporating liquid near its surface was measured with application of interferometry [19, 20] or thermometry [21, 22] techniques. The concept was that if the temperature profile was found to be linear, energy would be transmitted to the interface through thermal conduction. This means that there was no surface tension driven flow at the interface.

In contrast, by reducing the vapor-phase pressure using a vacuum pump, surface tension driven flow in pure water can be generated and is observable [13-15]. Duan and Ward [13-15] studied the evaporation process of pure water into its own vapor within a vacuum chamber. Since water has its maximum density at 4°C, they were able to conduct the investigation in the absence of buoyancy driven convection. The density of liquid water as a function of temperature is demonstrated in Fig.1-1. In the experiment of Duan and Ward, water was continuously supplied to a stainless-steel conical funnel to maintain the spherical water-vapor interface at a constant level as it evaporates at various high steady rates. The temperature at the bottom of the liquid phase was maintained at ~4°C. The temperature measurement using a 25μm diameter thermocouple revealed that there was a uniform temperature layer, which was resulted from the mixing induced by the Marangoni convection, at the surface of the evaporating water. The temperature profile beneath the uniform temperature layer was found to be linear and the temperature gradient was nearly constant. Depth of the uniform temperature layer, along with the evaporation rate, increased as the vapor-phase pressure was reduced. This indicated that Marangoni convection became more intense when the water evaporated at a higher rate. Furthermore, a 12.7μm diameter cantilevered probe was inserted into the liquid to measure the flow velocity at the liquid-vapor interface. The results were in accordance with the one calculated from the interfacial temperature gradients measured along the interface.

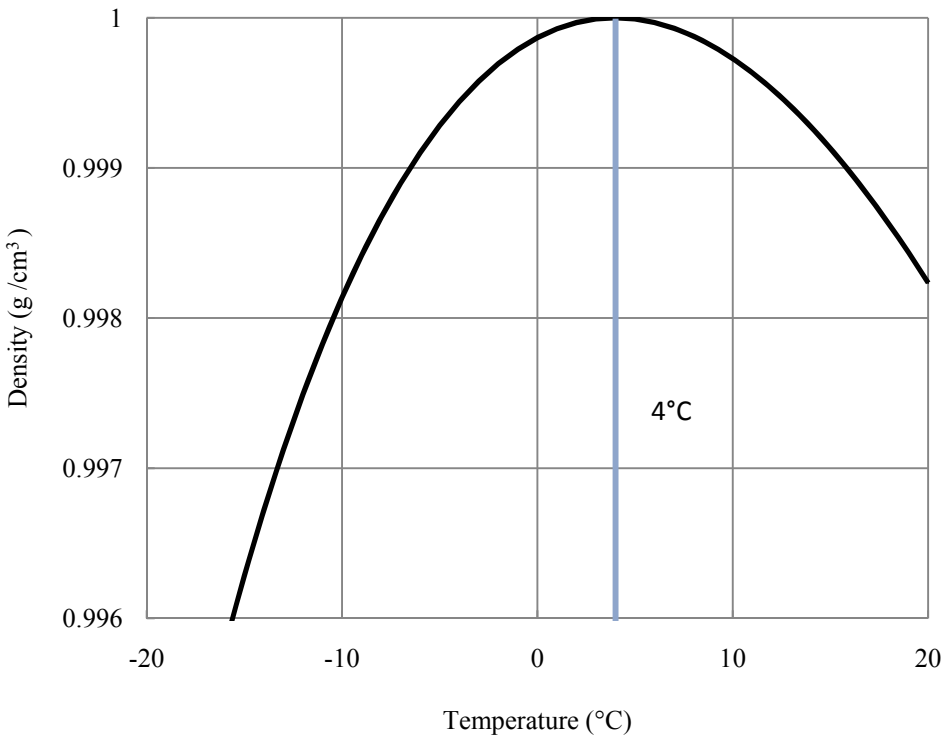

Figure 1-1. The density of liquid water as a function of temperature [2]

Duan and Ward have detected the Marangoni motion in water without visualizing the flow field. In contrast, Buffone and Sefiane [16-18] have visualized and characterized Marangoni convection in volatile liquids using micro-particle image velocimetry (micro-PIV). They investigated evaporation of the volatile liquids in still air. The liquids evaporated from their curved menisci formed in capillary tubes of various sizes. Strong convections beneath the interface were observed and visualized. The surface tension gradient, causing by the interfacial temperature variation induced by the non-uniform evaporation along the meniscus, was regarded as the driving mechanism for the convection. The evaporation induced convection was found to be correlated to the evaporation rate. An infrared camera was used to measure the temperature profile along the capillary wall and the meniscus. When external heating was applied to change the

interfacial temperature gradients along the meniscus, the convection pattern was altered and could be reversed. This revealed that the meniscus interfacial temperature profile played a key role for inducing the observed Marangoni convection.

Motivated by the findings of the previous research that were introduced above, the present study was devoted to experimentally investigating the evaporative convection in water in the absence of buoyancy driven motion. In order to determine the driving mechanism and property of the convection, velocity and temperature fields of the evaporative convection need to be measured. In the experiment, water was injected to a rectangular cuvette which was placed within a vacuum chamber. A vacuum system was designed to enable the water to evaporate at different high steady evaporation rates from its meniscus surface formed in the cuvette so that surface tension driven convection can be generated. A temperature controlling system was also designed to ensure that no buoyancy driven-convection would occur. Stereo-PIV was applied to visualize and characterize the convection field. The relation between the evaporation rate of water and strength of the expected convection was determined. Repeatability and time-dependence of the convection was also examined. To ascertain the driving mechanism of the expected convection, a temperature measurement on the centerline of the cuvette along with the stereo-PIV investigation was performed using a thermocouple probe. In addition, a PLIF investigation would also be applied to obtain the two-dimensional (2-D) temperature distribution in the bulk water.

1.2 Marangoni number calculation

To better understand the observed flow phenomenon, *Ma*, the key parameter for onset of the surface tension driven convection, needs to be quantitated. The method of

calculating *Ma* was first proposed by Pearson [10]. It is explained above and the calculating formula for *Ma* is shown in Eq. 1-1. For a specific liquid, water in this case, the surface tension γ, the dynamic viscosity η and the thermal diffusivity α are water properties that are function of temperature. They can be determined once the temperature is measured. However, the characteristic length *D* has to be determined based on the specific experiment. In Pearson's theoretical model, the layer thickness was considered as the characteristic length.

In the case of evaporation of a liquid from meniscus in a capillary, Buffone and Sefiane [16] estimated *Ma* for their theoretical model. In the study, volatile liquids evaporated from their curved menisci formed in capillary tubes of various sizes. The temperature in the center of the liquid surface meniscus was assumed to be same as the bulk liquid whose temperature was taken equal to the ambient temperature. Meniscus arc length between the wedge and the center of the meniscus was regarded as the characteristic length.

In contrast, Ward and Duan [13] investigated the evaporation process of pure water within a conical funnel. The water-vapor interface was maintained at just outside of the funnel mouth and was assumed to be spherical. The temperature was kept constant at the funnel throat and reduced with the height in the bulk water due to the cooling effect of evaporation at the water surface. The temperature profile on the centerline of the funnel in the liquid phase was found to be linear except for the uniform temperature layer right beneath the water surface. The thickness of the uniform temperature layer was exceptionally small while compared with the funnel size. For calculating *Ma*, they

considered the distance from the funnel throat to the liquid-vapor interface on the centerline as the characteristic length [3].

In conclusion, the characteristic length *D* needs to be determined according to the specific experiment.

1.3 Meniscus surface

Studies [16-18, 24] on evaporation of a liquid from a meniscus in a circular capillary have demonstrated that the extended meniscus can be divided into three regions, i.e., a macro region, a micro region and an adsorbed film region. These regions are illustrated in Fig. 1-2. It is known that a large portion of the evaporation from the meniscus occurs in the micro region where the liquid-vapor interface approaches the wall. Experimental study [24] has also shown that local temperature in the micro region is the lowest among these three regions because of its strongest evaporation flux.

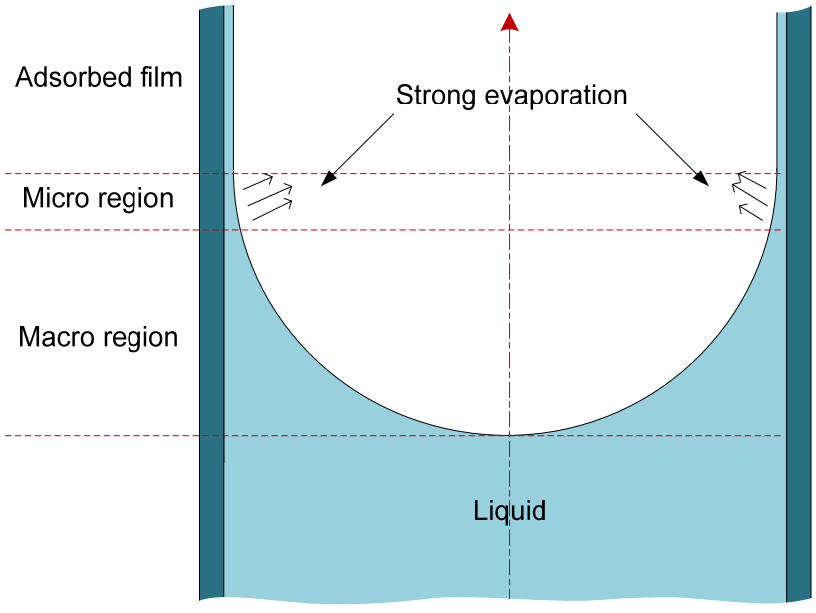

Figure 1-2. Schematic of the meniscus surface formed in a capillary tube

Different from the circular capillary, there are four corner menisci in addition to the bulk meniscus for the case of a rectangular capillary cuvette. Chauvet et al. [25] investigated the temperature distribution on the wall of a square capillary tube with a cross-section of 1mm×1mm using infrared thermography. The results showed that the temperature on the meniscus surface was the lowest at the tip of the corner meniscus and kept increasing towards the liquid bulk, indicating that the maximum local evaporation flux occurred at the tip of the corner meniscus. It was also noticed that the evaporation rate is much greater than a circular capillary tube due to the capillary pumping through the corner films which brings the location of the phase change much closer to the tube entrance.

The cuvette used in the present study has an inner cross-section of 4mm×10mm which was much larger than the square capillary tube that was used by Chauvet et al. [25]. However, the meniscus which is similar to that in the rectangular capillary tube was also observed. Accordingly, it is reasonable to expect that temperature variation along the meniscus surface of the water could be generated during evaporation. The surface tension gradient induced by the temperature variation might be able to drive a motion in the bulk water. To ascertain this, the velocity and temperature field in the bulk water needed to be measured.

1.4 Stereo- Particle image velocimetry

1.4.1 Principles

Particle image velocimetry (PIV) is an instantaneous, non-intrusive flow velocity measurement technique which has been well developed in the last three decades [26]. It measures flow velocity by tracking the displacement of reflective tracer particles that are

seeded into the fluid. A camera is used for collecting reflected light from the tracer particles to determine their positions. The recorded images are sub-divided into interrogation windows. The displacement of the particles can be calculated by comparing the interrogation windows in consecutive images. The velocity vectors can be determined by dividing the displacement with the known time delay. In a stereo-PIV experiment, rather than one single camera, two CCD cameras are needed to collect reflected light from different viewing angles on the same side of the light sheet. The two cameras can capture the projections of the velocity vector in two different planes. Since the positions of both cameras are known, all three components of the velocity vectors can be determined.

1.4.2 Literature review

PIV was developed from laser speckle velocimetry (LSV) which was originally used in solid mechanics and was then adapted to the measurement of fluid velocity fields [26]. It was first distinguished from LSV by Adrian [27] and Pickering and Halliwell [28] who identified that the low seeding density mode of LSV should be classified as PIV. Willert and Gharib [29] improved the PIV by using videographic recording other than photographic recording, enabling the data processing step to be simplified. The direction of the velocity vector can be determined easily by applying local spatial cross-correlations between two sequential single-exposed particle images.

In order to extend the application of the PIV to a 3-dimensional (3-D) velocity measurement, Willert [30] designed a PIV system that utilized two cameras which had a stereo configuration to recover the out-of-plane velocity component. This stereo-PIV technique was successfully applied to the investigation of an unsteady flow field of a

vortex ring passing through a laser sheet. Prasad and Adrian [31] studied the 3-D velocity vectors of the thermal convection in a large-aspect-ratio container of water using stereo-PIV. By comparing the 3-D velocity vector field and its corresponding 2-D projection, they concluded that the 2-D projection could lead to erroneous interpretation of the flow structure. This indicated that stereo-PIV is a more effective technique compared with 2-D PIV for investigating the fluid motion.

Buffone and Sefiane [16-18] have applied PIV to micro-scale fluid velocity measurement. They have visualized and characterized the Marangoni convection in volatile liquids that were evaporating from their curved menisci formed in capillary tubes in still air.

1.5 Planar laser induced fluorescence

Application of PLIF allows measuring the 2-D temperature profile of a liquid without disturbing. As a result, it was utilized to investigate the temperature distribution of the expected convection in water.

1.5.1 Principle

The PLIF technique is based on fluorescence of fluorescent dye molecules [32]. A fluorescent dye molecule can be excited by absorbing photons when exposed to laser light. This will result in electronic transitions in the molecule, causing the potential energy of the molecule to increase from the ground state to the first electronic excited state. When the potential energy of the molecule returns back to the ground state, fluorescence light will be emitted. The fluorescence intensity generated per unit volume can be expressed as:

$$I_f = I_0 \varepsilon C Q \tag{1-2}$$

where, I_f is fluorescence intensity, I_0 is laser intensity, ε is molar absorptivity of the dye, C is dye concentration, and Q is quantum efficiency.

The temperature dependence of the molar absorptivity, ε, is small and negligible in comparison with the temperature dependence of the quantum efficiency, Q, which is defined as the ratio of the total energy emitted per quantum of energy absorbed by the molecule. The change in fluorescence intensity can be as low as 0.13%/°C for a non-temperature sensitive dye, rhodamine 110 (Rh110), and as high as 2.3%/°C for a temperature-sensitive dye, rhodamine B (RhB). Therefore, the fluorescence intensity can be used to indicate the temperature by keeping the laser intensity and dye concentration constant. However, when applying PLIF to a temperature measurement, the laser intensity can be affected by various issues, including laser power fluctuation and non-uniform intensity distribution on the laser sheet generated from a laser beam.

To eliminate the constraint of the laser intensity variation, the two-color/two-dye PLIF was developed [32]. For application of the two-color/two-dye PLIF, both a temperature-sensitive-dye and a non-temperature-sensitive-dye are needed. The emitted fluorescence light from the two dyes needs to be split up and collected by two cameras separately. The fluorescence intensity of RhB is expressed as:

$$I_{RhB} = I_{0RhB} \varepsilon_{RhB} C_{RhB} Q_{RhB} \tag{1-3}$$

The fluorescence intensity of Rh110 is described as:

$$I_{Rh110} = I_{0Rh110} \varepsilon_{Rh110} C_{Rh110} Q_{Rh110} \tag{1-4}$$

The fluorescence intensity ratio of these two dyes is:

$$\frac{I_{RhB}}{I_{Rh110}} = \frac{I_{0RhB}\varepsilon_{RhB}C_{RhB}Q_{RhB}}{I_{0Rh110}\varepsilon_{Rh110}C_{Rh110}Q_{Rh110}} \tag{1-5}$$

Taking the ratio of the fluorescence light, dependence on the laser intensity of the measurement is eliminated because the same laser source is used. As a result, once the ratio of the concentration of the fluorescent dyes is fixed, the two-color/two-dye PLIF can be easily applied to a temperature measurement.

1.5.2 Literature review

PLIF (or planar LIF) is LIF that utilizes a laser sheet instead of a laser beam as a light source. The laser sheet is typically thin, making it possible to measure two-dimensional (2-D) temperature distribution [32-36]. The LIF technique has been well developed for measuring temperature profile as well as concentration in a fluid [36]. According to the difference in quantity of fluorescent dyes and cameras that were used, the LIF techniques are categorized and explained in the following sub-sections. In this study, two-color/two-dye PLIF was applied as the temperature measurement technique.

1.5.2.1 Single-color/single-dye

One way of applying the LIF technique to temperature measurement is referred to as the single-color/single-dye technique [32, 37-40]. It utilizes a single dye for temperature sensing and a single camera for fluorescence intensity measurement. Dye concentration and laser intensity are kept as constant so that the fluorescence intensity only depends on temperature. The temperature profile in the fluid to be investigated can therefore be measured by detecting the intensity of the fluorescence light emitted from the dye mixed in the fluid.

Temperature sensitivity of the dye serves an important part for application of the technique. The more sensitive is the dye, the better is the signal that can be obtained. RhB is considered as a suitable temperature indicator, because its temperature sensitivity can reach up to 2.3%/ °C [32], and its absorption spectrum covers a wide range [41], which means that the dye can be excited easily.

There are several constraints that limit the applicability and accuracy of the single-color/single-dye technique. When applying to investigations, both the dye concentration and the local laser intensity in the fluid need to be kept constant. Fluctuation of the laser power will induce systematic error which needs to be corrected by monitoring the laser power [36]. For the case of PLIF, the laser intensity needs to be uniform over the laser sheet. However, the laser has a Gaussian distribution in its cross-section and decays as propagating due to the absorption of the dyes dissolved in the fluid. Therefore, an image should be taken under the condition of constant dye concentration and uniform temperature for sheet correction [42].

Application of this technique had been extended by Hishida and Sakakibara [34] who combined the PLIF technique with the PIV technique for measuring both temperature and velocity simultaneously in a fluid. In the experiment, the laser beam was switched to a laser sheet by a cylindrical lens for illuminating, fluorescent dye and tracer particles were mixed in the fluid to be investigated, and two CCD cameras were used for recording the fluorescence light and particles' scattering respectively. This combined technique has been proved to be applicable for clarifying the heat transfer and turbulent characteristics of the stratified flow, as well as natural convection and the plane impinging jet.

1.5.2.2 Two-color/two-dye

Different from the single-color/single-dye LIF technique, the two-color/two-dye LIF technique employs two different fluorescent dyes and collects fluorescent light in two selected spectral bands. The selected dyes share similar absorption spectra but different emission spectra. This enables them to be excited by the same laser and their emitted light to be collected separately using appropriate light filters. Since one of the fluorescent dyes is sensitive to temperature while the other one is not, their fluorescence intensity ratio indicates temperature and is independent of intensity of the incident laser sheet [32]. Therefore, by keeping the concentration ratio of the dyes constant, fluorescence intensity ratio only depends on temperature. This technique improved the measurement accuracy and reduced systematic error.

Many researchers have applied the two-color/two-dye LIF technique in their study of flow phenomenon [32, 35]. RhB and Rh110 are the most popular dyes. RhB is a temperature-sensitive dye, and Rh110 is a non-temperature-sensitive dye whose temperature sensitivity is as low as 0.13%/°C [32]. Sakakibara and Adrian [32] utilized this technique in their study of instantaneous 3-D temperature measurement in water. In the experiment, they measured the 3-D temperature profile of thermal convection from a horizontal surface with uniform heating by scanning the planar laser sheet over the thermal convection field. They tested the effect of quenching and found that the fluorescence of Rh110 decreased exponentially after the excitation started, and that the fluorescence of RhB had the same tendency but degraded much slower than that of Rh110. Glass equipment was suggested for the actual experiment because it does not induce any impurity which could influence the fluorescence intensity. In contrast, fluoropolymer equipment can cause the fluorescence intensity to decay rapidly.

Kim et al. [35] have adopted the two-color/two-dye LIF technique for measurement at micro-scales. Their results indicated that this technique can be successfully used as a micro-scale temperature mapping tool, and that it is possible to get more accurate data with better experimental equipment, such as a CCD camera with more pixels. It was found that the measurement uncertainties are inversely proportional to interrogation cell sizes in the image processing procedure. To decrease the effect of photo-bleaching of dyes, they suggested using fresh mixtures of dyes less than two or three days old.

1.5.2.3 Two-color/single-dye

The two-color/single-dye technique eliminated the constraint on concentration ratio of the dyes. It requires one dye to indicate temperature and two cameras to record fluorescence light in two different spectral bands. According to Lavieille et al. [43], the temperature sensitivity of the RhB spectrum is considerably dependent on the wavelength. Two spectral bands with highly different temperature sensitivities can be selected, one of which is sensitive to temperature while the other is not. The ratio of the fluorescence light intensities collected in these two spectral bands depends on temperature only.

This technique was first introduced by Lavieille et al. [43, 44] who applied it to the mean droplet temperature measurement of evaporating and combusting droplets in a monodisperse spray. They had discovered that the difference between re-absorption of the two spectral bands could lead to error for the case of large optical paths. Bruchhausen et al. [36] have developed the technique by applying it to temperature measurement on a heated turbulent jet injected into a coflow at ambient temperature. They calculated the instantaneous and mean temperature profiles in the fluid and compared them with the

results obtained from using the single-color/single-dye technique. It was found that the previous results are much better. The investigation revealed that the different re-absorption of the two spectral bands does not have a strong influence on the sensitivity of the fluorescence intensity ratio to the temperature.

1.5.2.4 Three-color/single-dye

To overcome the problem caused by re-absorption, Lavieille et al. [45] introduced the three-color/single-dye LIF technique and clarified the capability of the technique by measuring the temperature in a heated liquid jet. The difference between the three-color/single-dye technique and the two-color/single-dye technique is that the former requires a third spectral band to take the fluorescence re-absorption phenomenon into account. The first spectral band is insensitive to temperature but sensitive to re-absorption, the second one is the converse, and the last one is sensitive to both. RhB was selected as the fluorescent dye. Three fluorescence intensities of the spectral bands were measured and used to determine temperature. This technique eliminated the dependencies on dye concentration, the local laser intensity and the fluorescence re-absorption effects.

1.6 Thesis outline

This thesis is an experimental based research that aimed to study the motion arising in density stabilized water due to evaporation. A hypothesis is that the motion is driven by variations in surface tension induced by temperature gradients which are caused by non-uniform evaporation flux along the water surface. To investigate the driving mechanism of the evaporative motion, the velocity and temperature field of the motion need to be measured. The thesis includes 6 Chapters and 1 Appendix. Chapter 1 reviews the previous related literatures. Chapter 2 introduces the experimental setup used

in the experiment and the preparation procedure for the experiment. Chapter 3, 4 and 5 describe different experiments using various techniques for investigating the evaporation induced convection beneath the liquid-vapor interface in the liquid water. Chapter 6 summarizes the experimental results and concludes diving mechanism of the observed convection. The Appendix demonstrates drawings of the components of the vacuum chamber system. The thesis includes the following chapters.

Chapter 1: Literature reviews of the Marangoni convection and overview of the stereo-PIV and the PLIF techniques are presented in this chapter. The motivation is explained and a brief introduction of this thesis is presented.

Chapter 2: This chapter introduces the experimental setup and preparation procedures for the investigation. The first subsection describes the designed vacuum system, which is able to control pressure and temperature, and measurement devices for monitoring the experiment conditions. The imaging system for application of both the stereo-PIV and the PLIF investigation are presented subsequently. Lastly, the experimental preparation procedure is explained in detail.

Chapter 3: In this chapter, temperature measurement using a thermocouple probe during the stereo-PIV investigation is introduced. The experimental procedure and obtained temperature profiles at different experimental conditions are described. Sources of error that could reduce the accuracy of the measurement are discussed. Marangoni number as a key parameter for onset of Marangoni convection is analyzed based on the temperature results.

Chapter 4: Stereo-PIV measurements of the flow field velocity are investigated in this chapter. The procedure of the stereo-PIV investigation is detailed. Velocity fields of the observed convection at different evaporation rates are calculated and discussed.

Chapter 5: This chapter focuses on application of the PLIF technique to a 2-D temperature profile measurement of the observed convection shown in Chapter 4. The selection of dyes and spectral bands of the emission light to be collected are revealed. The calibration method of the PLIF and the actual experiment are described in detail. Results are illustrated and the possible sources of error are analyzed.

Chapter 6: This chapter summarizes the experimental results and concludes a driving mechanism for the observed evaporative convection of water. A discussion of future work is also included.

Appendix: Drawings of the copper block, Teflon gaskets and support plates are provided in this appendix.

CHAPTER 2 : EXPERIMENTAL SETUP AND METHODOLOGY

In this thesis, two different measurement techniques were applied to investigate the evaporative flow in the bulk water. They are stereo-PIV for visualizing the flow field and PLIF for measuring the 2-D temperature profile of the bulk field. In addition, a direct temperature measurement in the flow field using a thermocouple was also implemented along with the stereo-PIV experiment.

In order to perform these investigations, an experimental setup consisting of a vacuum system and an imaging system was designed. The vacuum system can generate an environment in which the pressure and temperature can be controlled. This was used to induce an evaporative flow by controlling the evaporation rate of the liquid water. The imaging system was designed for application of both the stereo-PIV and the PLIF techniques. These experimental setups are detailed in this chapter. In addition, the preparation procedure of the experiments is also described in this chapter.

2.1 Experimental setup

In the investigation, a quartz cuvette (9F- Q- 10, Starna Cells) was chosen as the experimental liquid container. All walls and the base of the cuvette were optically polished and therefore remain extremely flat, allowing the cuvette to be suitable for laser

and imaging techniques. As can be seen in Fig. 2-1, the horizontal cross-section of the cuvette is a uniform rectangular from the bottom till near the top end where it becomes wider and has a V-shape. Table 2-1 details the physical and optical specifications of the cuvette.

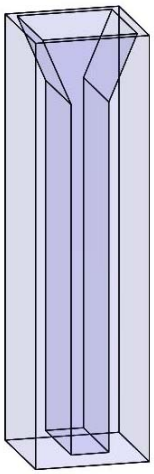

Figure 2-1. Schematic of the cuvette

Table 2-1. Specifications of the cuvette

Model	Interior width	Interior length	Height	Material	Useable spectrum range
9F- Q- 10, Starna Cells	4 mm	10 mm	45 mm	Quartz	170- 2700 nm

At the beginning of each experiment, the cuvette would be filled up with the liquid to be investigated. Since the liquid was not continuously supplied to the cuvette during the experiment, the liquid-vapor interface would drop as evaporation of the liquid takes place. To avoid the effect of the V-shape funnel on the expected flow, all the data

were collected when the meniscus of the liquid-vapor interface was below the bottom edge of the V-shape funnel.

The evaporation process of the experimental liquid took place in a vacuum chamber (CU6-0275, Kurt J. Lesker) in which the pressure was controllable. An image, Fig. 2-2, and a schematic, Fig. 2-3, illustrate the experimental configuration including the vacuum chamber system and the imaging system. As shown in the figures, the vacuum chamber was connected to a vacuum pump. An angle valve was equipped between them to control the pressure within the vacuum chamber. A pressure transducer (PX419-005A5V, OMEGA) was installed between the angle valve and the vacuum chamber in order to monitor the vacuum chamber pressure. An analog signal from the pressure transducer was converted to a digital value by a data acquisition system (Minilab 1008, Measurement Computing Corporation) that was connected with a PC and controlled using custom software (LabWindows/CVI, National Instruments). The software code provided a visual panel which enables monitoring of the instantaneous pressure. Four flanges with quartz windows were installed as side walls of the chamber, allowing the liquid inside the cuvette to be optical accessible.

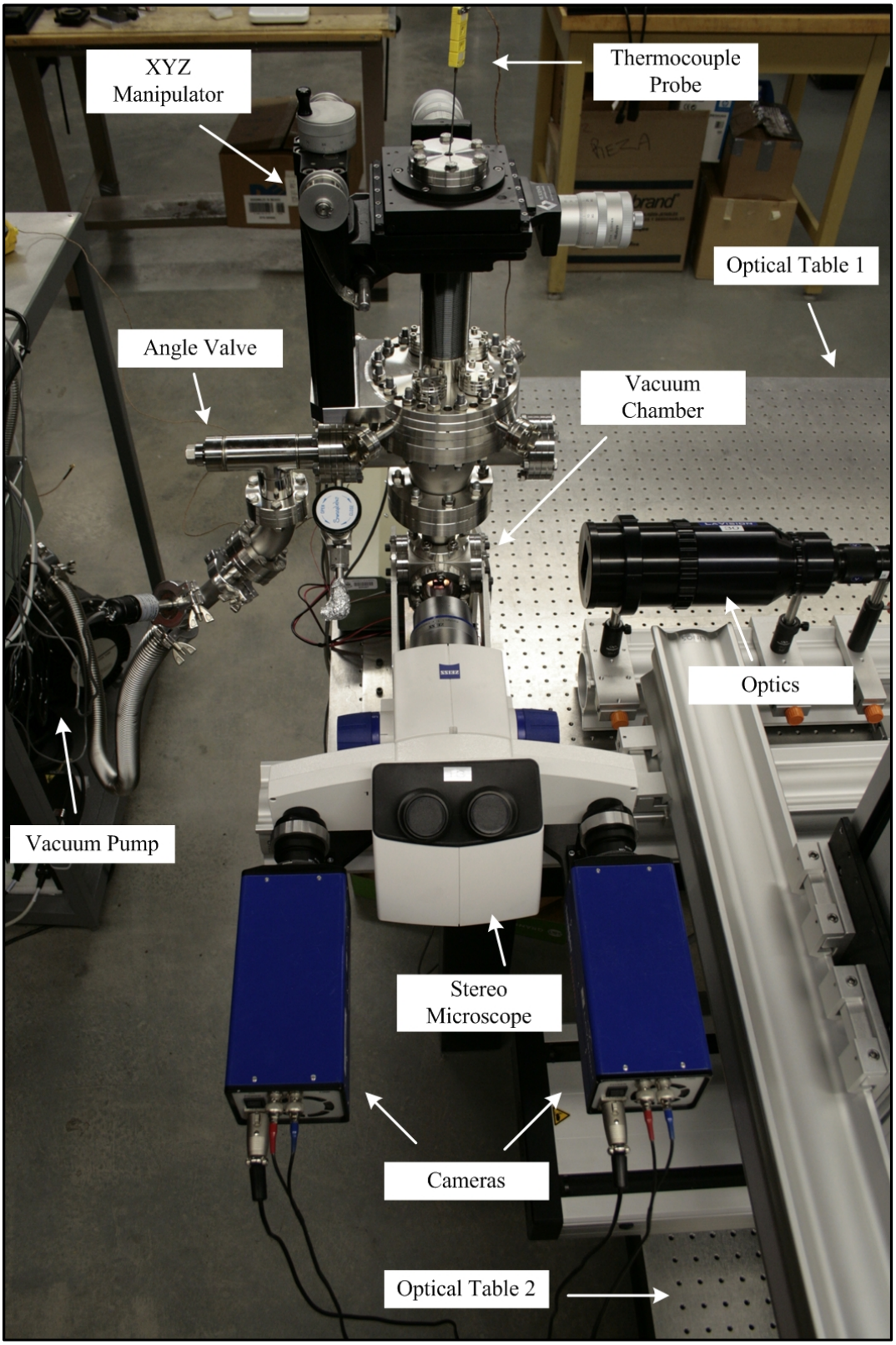

Figure 2-2. Picture of the experimental setup

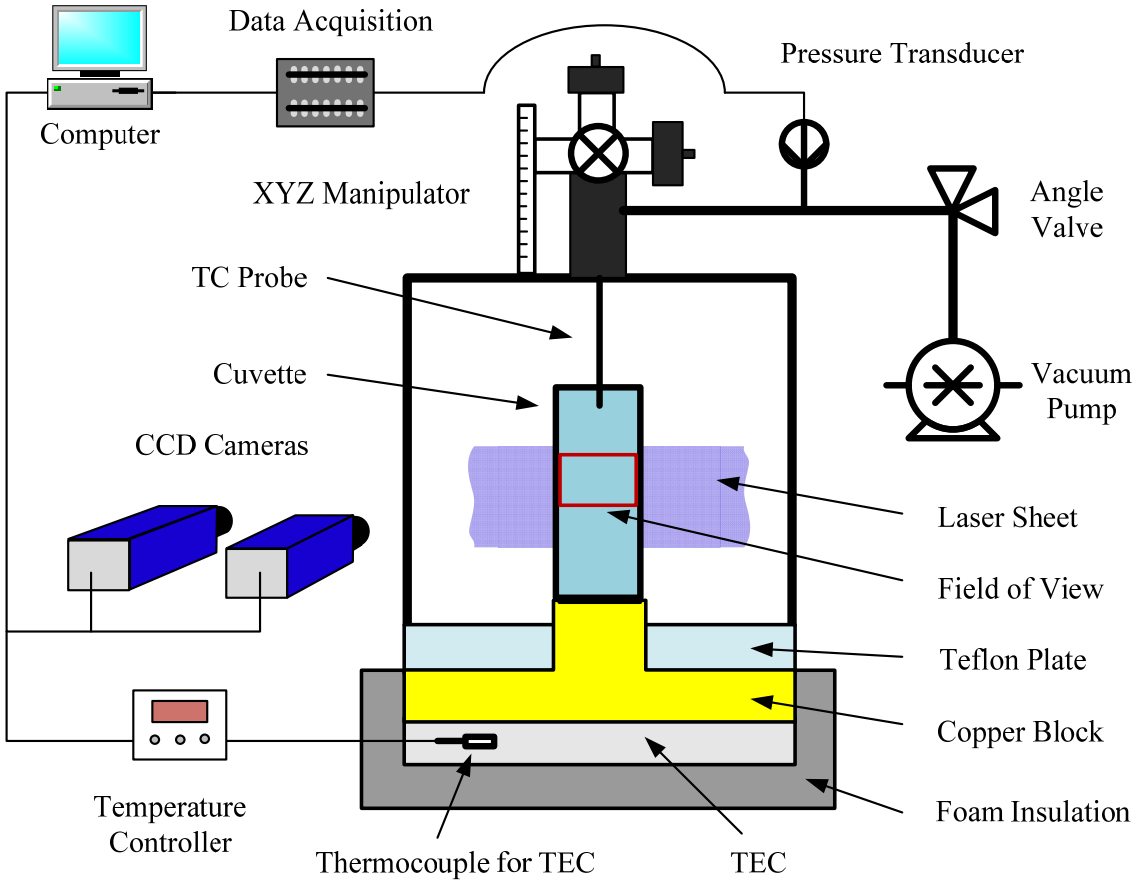

Figure 2-3. Schematic of the experimental setup

In order to eliminate buoyancy driven flow in the liquid phase within the cuvette, the temperature profile in the liquid bulk needs to be controlled. To achieve this, a specialized experimental configuration for the vacuum chamber was designed and is showed in Fig. 2-2, Fig. 2-3 and Fig. 2-4. The bottom of the vacuum chamber was sealed by a Teflon flange, which has a similar structure to other flanges but is thermally isolated, and a copper block, which has excellent thermal conductivity. A thermoelectric cooling device (TEC, CP-031, TE TECHNOLOGY) was joined to the copper block by

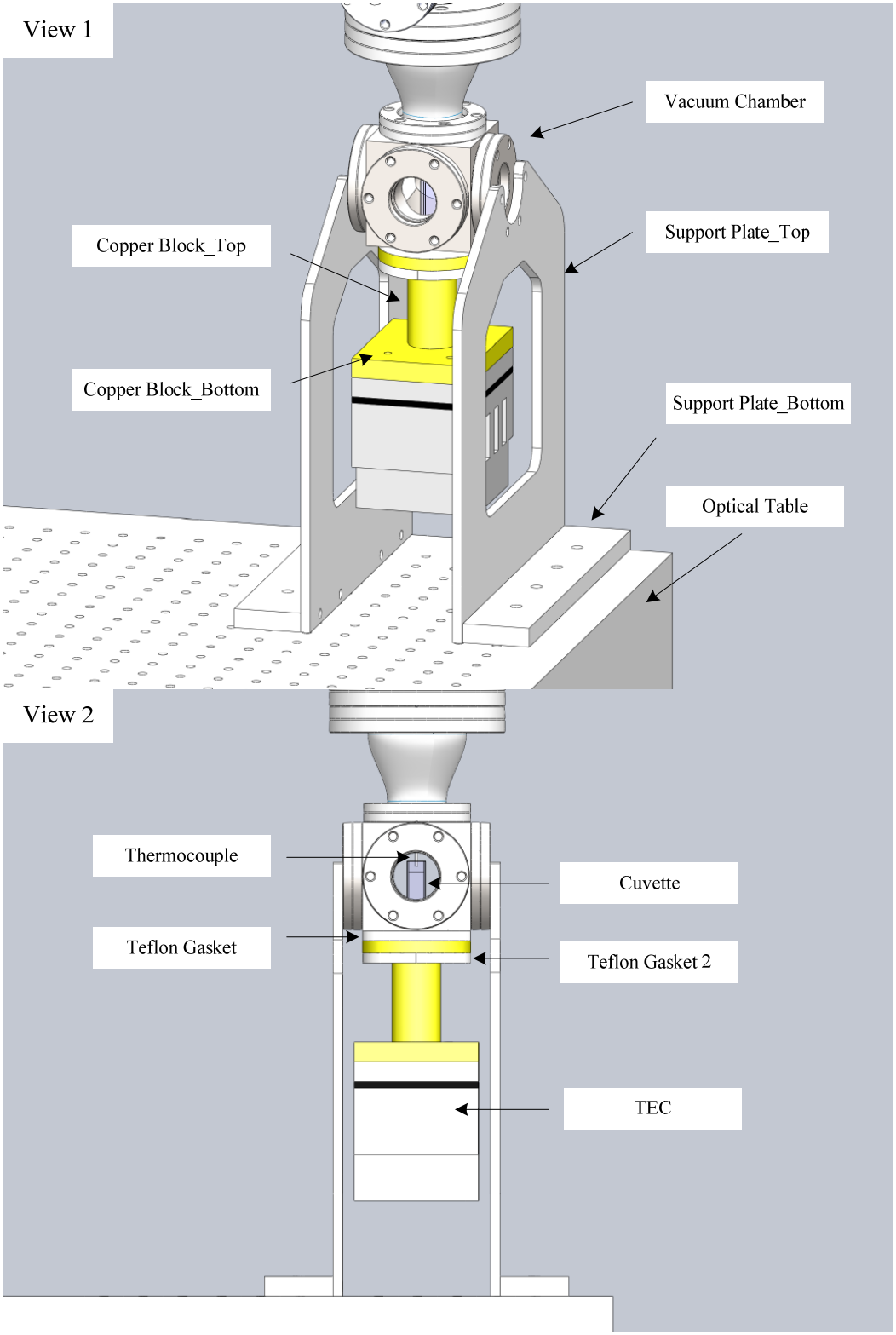

Figure 2-4. Image of the 3-D model of the vacuum chamber system

screws. It can be operated through a temperature controller (TC-36-25, TE TECHNOLOGY) by using provided commercial code which allows monitoring and communicating with the TEC. Foam was used for external wrapping to reduce the heat exchange between these devices and the atmosphere. The cuvette was placed in a groove on the top of the copper block, and thermal paste was used to improve the thermal contact between them. The TEC has heat exchange mainly with the cuvette through the copper block and was able to control the temperature at the bottom of the cuvette. The TEC has a wide temperature range of -20°C to 100°C. Details on the equipment that was designed for vacuum sealing and temperature control are illustrated by drawings in the Appendix.

As the vacuum chamber was sealed and inaccessible from outside, in order to implement temperature measurement within the cuvette, a specialized thermocouple feedthrough probe was attached to an XYZ manipulator (RX100, Kurt J. Lesker) which was equipped on the top of the vacuum chamber. By operating the XYZ manipulator which has a resolution of 0.005 mm, the thermocouple was able to reach any position inside the cuvette because the XYZ manipulator has three translational degrees of freedom. The specifications of the thermocouple feedthrough probe are listed in Table 2-2. A portable digital thermometer (HH506A, OMEGA) was used for readout from the thermocouple. For positioning of the thermocouple probe, a cathetometer (3383-A, GAERTNER) which has a resolution of 0.01 mm was employed for observing. It can determine the position of the end of the thermocouple probe relative to the cuvette.

Table 2-2. Specifications of the thermocouple probe

Thermocouple type	Temperature range	Probe diameter	Probe length	Encasing material
K	-200°C to 1250 °C	1.55 mm	18 inches	Stainless steel

2.2 Imaging system

2.2.1 Overview of the imaging system

An imaging system, which mainly includes the laser, optics and cameras, was designed for both stereo-PIV and PLIF investigation. Its alignment is shown in Fig 2-5. A laser beam emitted by the laser was reflected to the sheet forming optics by a mirror. A beam expander with a magnification of 4.2× was used to expand the diameter of the laser beam. The expanded laser beam was then transformed into a thin laser sheet by the light sheet optics and the collimator optics which were mounted next to the beam expander. The experimental liquid inside the vacuum chamber can be illuminated by the laser sheet and be observed by the CCD cameras (Imager Intense, LaVision) that were mounted on the stereo microscope (SteREO Discovery.V8, ZEISS). The reason for using the microscope was because both the stereo-PIV and the PLIF investigation need two views for observing the experimental liquid.

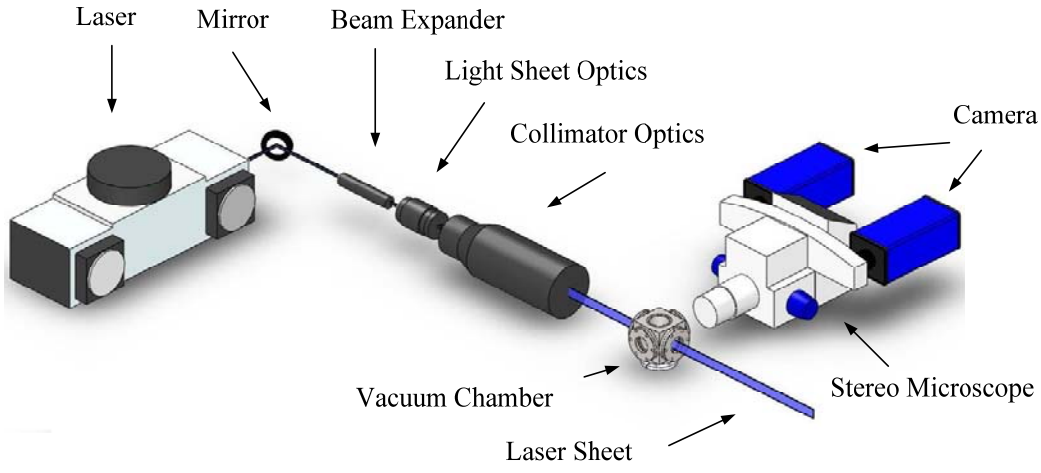

Figure 2-5. Layout of the imaging system

Two different lasers were used in the experiment, that is, a semiconductor diode laser for stereo-PIV and an Argon ion laser for PLIF. Specifications of the laser are detailed in Table 2-3.

Table 2-3. Specifications of the lasers

Laser model	Laser type	Wave-length	M^2	Beam diameter	Beam divergence	Output power	Output type
5500AWC	Argon ion	488 nm	~1.2	0.82 mm	0.78 mrad	100 mW	CW
Green Hercules	Semiconductor diode laser	532 nm	N/A	< 1.5 mm	0.8 mrad to 1.2 mrad	500 mW	CW

The sheet forming optics include beam expander, light sheet optics and collimator optics. The optics layout is displayed in Fig 2-6. For a given laser beam with a specific wavelength, the minimum thickness of the formed laser sheet is determined by the beam quality factor, M^2, of the original laser beam [46] and can only be obtained in a small region. The practical laser sheet thickness is its average value over the field-of-view (FOV) in the experiment. The obtained laser sheet thickness in this study was less than 0.5 mm. The distance between the lenses in the light sheet optics is adjustable, allowing the position of the focal plane to be adjusted. Likewise, the height of the laser sheet thickness is also controllable by changing the distance between the lenses of the collimator optics.

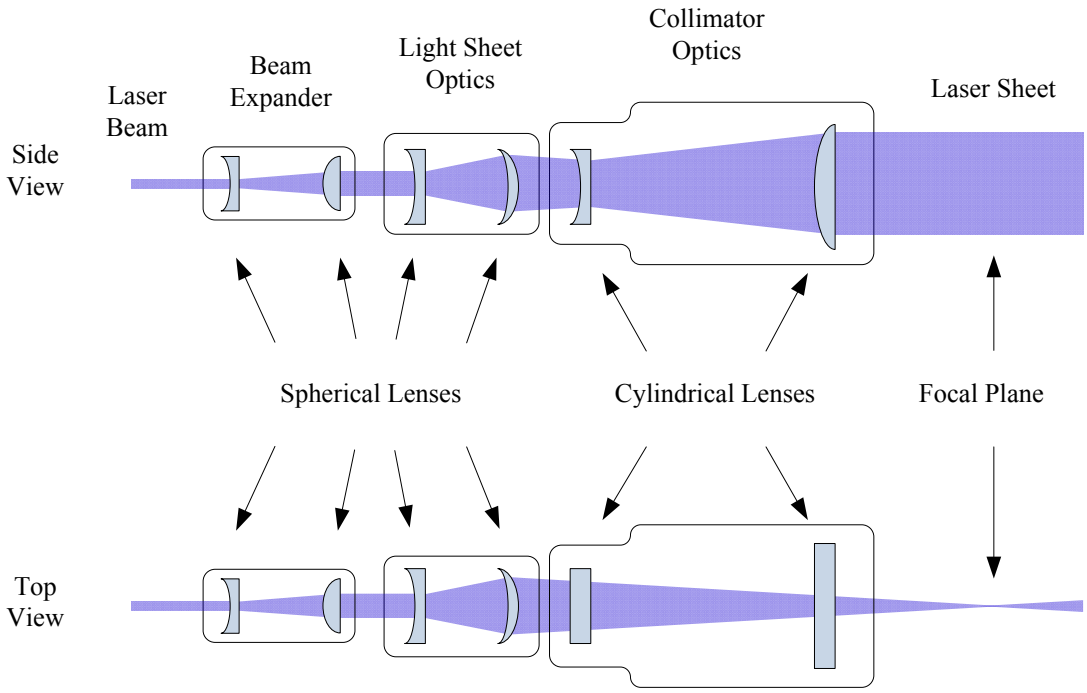

Figure 2-6. Layout of the optics

Light from the experimental fluid can be collected by the objective lens of the stereo microscope and split up into two light beams that are collected by two CCD cameras respectively. The camera views are in a stereo configuration with an included angle of 17.1° with respect to each other. Specifications of the CCD cameras are listed in Table 2-4.

Table 2-4. Specifications of the LaVision Imager Intense Camera

Exposure time	**Number of pixels**	**Pixel size**	**Sensor format**	**Spectral response**	**Maximum QE**
500 ns to 1000 s	1376 × 1040	6.45µm× 6.45µm	2/3"	280 nm to 1000 nm	65% @ 500 nm
CCD temperature	**Dynamic range**	**Scan rate**	**Readout frequency**	**Readout noise**	**CCD quality**
-12°C	12 bit	16 MHz	10 frame/s	4 e- to 5 e- @ 16 MHz	Grade 0

2.2.2 Imaging system for stereo-PIV

For the stereo-PIV investigation, PIV particles with a diameter of 2 μm (THERMO SCIENTIFIC) were used as flow tracers. The light scattered from the seeded particles in the experimental fluid was recorded by two CCD cameras in single-frame, single-exposure mode at a specific frequency. For a given expected exposure intensity of the images, the exposure time would be inversely proportional to the intensity of the reflective light of the seeding particles. In the case of high speed fluid motion, the projection of the PIV particles on the recorded images would be a trace instead of a dot if the exposure time is too long. This is because movement of the particles during the exposure time was captured in a single image. Therefore, a laser with high power can reduce the exposure time and result in clear images. The semiconductor diode laser with a power of 500mW was a proper choice for the light source. This allowed good quality images to be recorded with an exposure time of 0.02s during the investigation.

2.2.3 Imaging system for PLIF

For the PLIF investigation, an Argon ion laser (5500AWC, ION LASER TECHNOLOGY) was employed due to its small M^2 value, which is ~1.2, and proper emission wavelength, which is 488nm. Fluorescent dyes RhB and Rh110 (EXCITON) were used as temperature indicators. Fluorescence light emitted from the dyes dissolved in the experimental fluid was collected by CCD cameras in single-frame, single-exposure mode. Two light filters with different wavelength ranges were utilized to transmit the fluorescent light selectively according to its wavelength. They were placed in front of each camera.

In addition, a knife edge was used to cut off the laser sheet partially. It can be moved vertically to control the top edge of the transmitted laser sheet. This was to ensure that the laser sheet would go through the liquid at a position that is right beneath the meniscus surface. In this case, refraction of the laser light induced by crossing the meniscus surface can be avoided.

2.3 Experimental preparation

Water would be purified first before being used in the experiment. PIV particles were mixed in the purified water for stereo-PIV investigation. Similarly, fluorescent dyes were dissolved in the purified water to obtain a solution for PLIF investigation. The cuvette that was used as the liquid container was cleaned before being filled up with the suspension or solution. When the experimental apparatus was set up as in Fig. 2-3, degassing of the suspension or solution was performed, after which the experiment would be ready to implement. Details on the experimental preparation procedures are introduced in the following subsections.

2.3.1 Water purification

The water used in the experiments was distilled and de-ionized by a water deionization system (D4641, BARNSTEAD) so that the water properties would not be affected by impurity. The resistivity of the water to be used reached 18.2 MΩ-cm after purification.

2.3.2 Making the suspension and solution

The particles used for PIV were provided in a high-concentration suspension. A drop of the suspension was mixed with 40ml purified water before being used for the stereo-PIV investigation.

Two fluorescent dyes, RhB and Rh110, which are highly soluble and slightly soluble respectively, were dissolved in purified water as solvents to make solutions. An analytical balance (1207MP2, SARTORIUS) which has a resolution of 0.1mg was utilized for weighing. Water was distilled and de-ionized before being used as solute. In order to obtain a uniform concentration solution, a stirrer (PC-353, CORNING) was used to mix the solution. The prepared solutions were kept in glass bottoms with plastic covers and were stored in a dark place to avoid decay of the fluorescent dyes. Concentrations of RhB and Rh110 in the solution were 2.0mg/l and 0.25mg/l respectively.

2.3.3 Cleaning of the cuvette

Cleaning of the cuvette was implemented before its use each time in the experiment. The cuvette was first cleaned with detergent Alconox powder, and then rinsed with flowing pure water for at least one minute. For the PLIF investigation, to avoid influence of the possible remnant water on the concentration of the water solution, the cuvette was also rinsed with the dye solution several times after cleaning.

2.3.4 Degassing of the experimental liquid

To enable the experimental liquid, which was a water solution or suspension, to evaporate in steady-state at low pressure, degassing of the liquid had to be implemented in advance. During the degassing process, by adjusting the angle valve when the mechanical pump was turned on, the vacuum chamber pressure was reduced gradually

from atmospheric pressure to several hundred Pascal over approximately one hour. Visible bubbles could be seen to form and depart from the cuvette. Decrease of the vacuum chamber pressure need to be extremely slow because rapid pressure drop may cause excessive bubbles to form and escape the cuvette quickly, which would induce overflow of the liquid. After degassing, the gas within the vacuum chamber became water vapor only.

CHAPTER 3 : TEMPERATURE MEASUREMENT ON THE CENTERLINE OF THE FLOW FIELD WITH A THERMOCOUPLE

Since the purpose of the thesis was to study the Marangoni convection, it is important to ensure that the observed motion in the liquid to be investigated is induced by surface tension. However, buoyancy force is another cause that could result in a flow. The buoyancy force in the liquid is dependent on the water density which is a function of the temperature profile through the height of the water. A temperature measurement using a thermocouple is necessary to determine the driving mechanism of the observed flow. The measured temperature profile can also be used for estimating the key parameter of the surface tension driven convection, the Marangoni number.

3.1 Experimental procedure and conditions

The temperature measurement was implemented at the end of the stereo-PIV experiment (see Chapter 4). The reason for the timing was to avoid any affect of the disturbance induced by the thermocouple on the velocity field measurement. The bulk of the utilized thermocouple probe was large compared with the size of the cuvette in which the flow occurred. Therefore, the steady-state flow would be disturbed to some extent. The temperature measurement procedure was performed quickly over the course of ~1

minute to minimize measurement error. The setup for the experiment was illustrated in Fig. 2-3. In the experiment, the thermocouple probe was inserted into the water phase along the centerline of the cuvette from the liquid-vapor interface to the bottom of the cuvette. The XYZ manipulator and the cathetometer were used for positioning and monitoring respectively.

The vapor-phase pressure within the vacuum chamber was set at four different values which are 250 Pa, 450 Pa, 620 Pa and 820 Pa. The obtained average pressure was in a range of ±15 Pa around the set value. Under each condition, the temperature measurement, along with the stereo-PIV experiment, was repeated for three times to examine repeatability of the results.

3.2 Results and discussion

3.2.1 Results

The varying trend of the interfacial temperature on the centerline of the cuvette with respect to the vapor-phase pressure is shown in Fig 3-1. It can be seen that the temperature decreased as the pressure was reduced, which had also been observed by Ward and Duan [13-15]. The reasoning behind this variation is that the decrease of the vapor-phase pressure can increase evaporation flux of the liquid water, which requires more energy from the water surface and therefore decrease the interfacial temperature.

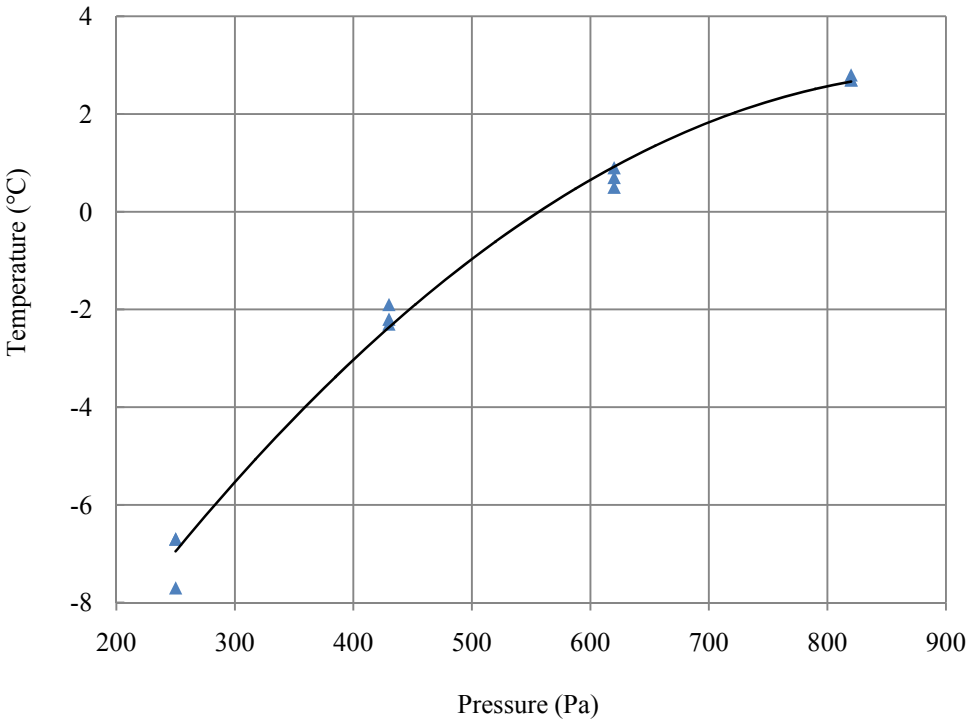

Figure 3-1. Interfacial temperature at the centerline of the meniscus surface versus vapor-phase pressure

The temperature profiles on the centerline of the cuvette at different vapor-phase pressures are shown in Fig. 3-2. The surface is denoted as 0 mm, and all locations below the surface are described by their depths which are their distances from the surface. As can be seen in the figure, the temperature increases linearly along the centerline of the cuvette from the water surface to ~12 mm below the water surface when the vapor-phase pressure were ~250 Pa, ~430 Pa and ~620 Pa. In contrast, when pressure was increased to ~820 Pa, the temperature increased smoothly from the water surface to ~9 mm beneath the surface, from where it becomes nearly constant till the bottom of the cuvette.

In conclusion, as the vapor-phase pressure varied from ~250 Pa to ~820 Pa, the temperature along the centerline of the cuvette was always decreasing with height, and

was lower than 4°C. According to the relation between water density and temperature that was shown in Fig. 1-1, the temperature profile indicates that the denser water was always below the lighter water, revealing that the water was density stabilized during the investigation.

The depths of the remaining water in the cuvette were not the same for different experiments when performing the temperature measurement using a thermocouple. This is because water was not continuously supplied to the cuvette to maintain the water surface at a fixed level. As the water evaporated, the water surface dropped for various displacements due to the difference in evaporation rate and experiment duration.

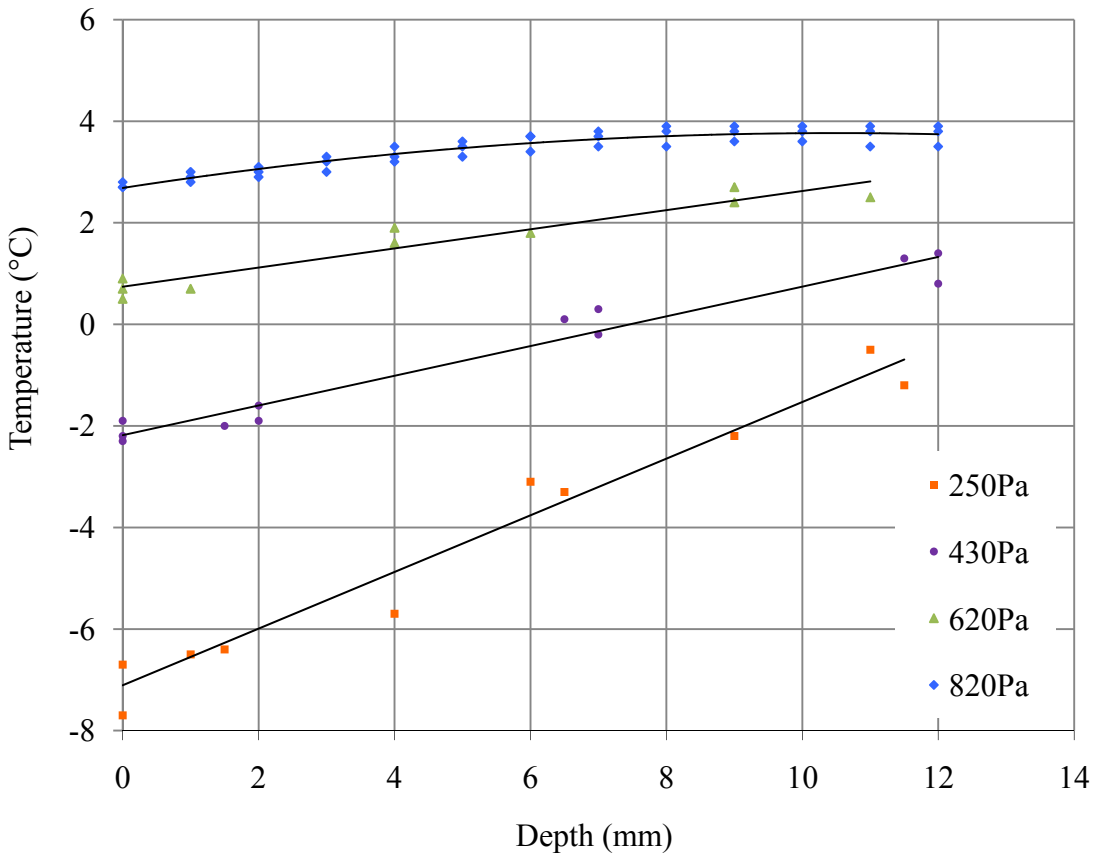

Figure 3-2. Temperature profile on the centerline of the cuvette at various vapor-phase pressures

3.2.2 Main sources of error

The main sources of error in the temperature measurement arose from the size and the structure of the thermocouple probe. Firstly, the thermocouple probe has a diameter of 1.55 mm which is large compared with the cuvette, the latter of which has an inner cross-section of 4mm×10mm. Therefore, it could disturb the flow field significantly. To minimize this error, the measurement procedure was finished within a short time. The thermocouple was moved to the next measuring point once the temperature reading became stable. However, since the thermocouple was encased in a stainless steel sheath which removed it from direct contact with the water, there would be a time delay which extended the measurement duration. Also, the thermocouple probe was contacted with water over a large area. The reading from the portable digital thermometer was thus the average temperature value across the contacted area.

3.3 Calculation of the Marangoni number

As discussed in Chapter 1, to calculate *Ma*, the characteristic length and the corresponding temperature profile need to be determined. In this investigation, the temperature profile on the centerline of the liquid bulk was measured whereas the temperature measurement along the meniscus surface was not resolved. The latter one is critical because it is believed that the evaporation of water can lead to temperature variations along the meniscus surface. As a result, an accurate value of *Ma* is not able to be obtained. However, it is still helpful to estimate the *Ma* using the centerline temperature profile.

The results showed in Fig. 3-2 indicated that the obtained temperature profiles are linear all the way except for the case of ~820 Pa vapor-phase pressure. However, for

estimating *Ma*, this temperature profile was regarded as linear approximately for simplification. The depths showed in Fig. 3-2, over which the temperature was investigated, were considered as the characteristic length.

If the surface tension is denoted by γ_{LV}, the temperature on the centerline at the liquid-vapor interface by T_{LV}, the temperature at the bottom of the liquid by T_B, the dynamic viscosity by η, the thermal diffusivity of the liquid by α_L, and the characteristic length by *D,* the Marangoni number can be expressed by expanding Eq. 1-1,

$$Ma = \left(\frac{\partial \gamma_{LV}}{\partial T} \right) \frac{(T_{LV} - T_B) D}{\eta \alpha_L} \tag{3-1}$$

The temperature profiles obtained at the same vapor-phase pressures were averaged first before being used for calculation. Based on the averaged temperature results, *Ma* was calculated at different vapor-phase pressures and is shown in Fig. 3-3. It can be seen that *Ma* increases smoothly from 8261 to 37503 as the pressure decreases from 820 Pa to 250 Pa.

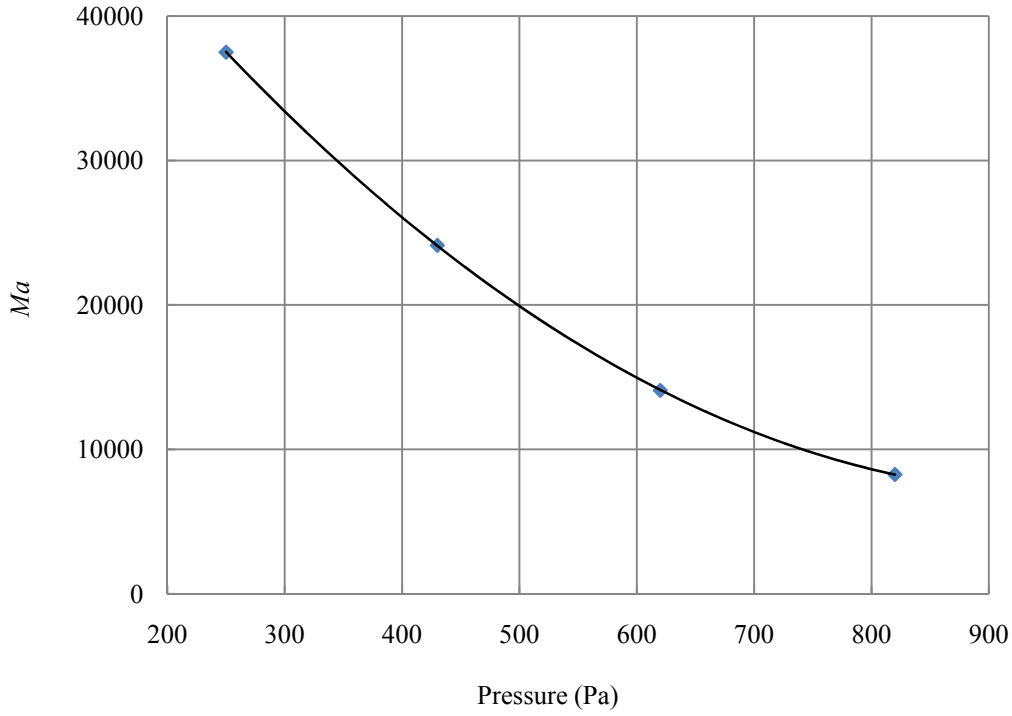

Figure 3-3. Relation between the vapor-phase pressure and the estimated Marangoni number

3.4 Conclusion

The thermocouple temperature measurements were performed along with the stereo-PIV investigation as the vapor-phase pressure varied from ~250 Pa to ~820 Pa. It was observed that the column of water was density stabilized on the centerline of the cuvette for the conditions investigated.

The Marangoni number was also estimated. For the conditions investigated, *Ma* was found to be considerably greater than the critical value, 80, for onset of Marangoni convection. In addition, the Marangoni number was dependent on the vapor-phase pressure. It increased as the vapor-phase pressure was reduced.

CHAPTER 4 : VISUALIZATION OF EVAPORATION INDUCED FLOW IN WATER USING STEREO-PIV

To investigate the expected evaporation-induced motion in water, velocity and temperature field in the bulk water need to be measured. Knowledge of the velocity field will also indicate the energy transfer mechanism for evaporation. Therefore, stereo-PIV was applied to visualize and characterize the flow field in the water. Besides, as described in Chapter 3, a temperature measurement was performed along with the stereo-PIV investigation using a thermocouple probe.

4.1 Experiment conditions

The experimental setup for the stereo-PIV investigation was illustrated in Fig. 2-2 to Fig. 2-5 and was described in Chapter 2.

In order to determine dependence of the evaporative motion on vapor-phase pressure, four sets of experiment were performed at different vapor-phase pressures within the vacuum chamber, which were 250 Pa, 450 Pa, 620 Pa and 820 Pa. Each set included 3 repeated experiments to examine repeatability of the results. The obtained average pressure ranged by ±15 Pa around the set value. The set point of the TEC was 4°C throughout the experiment.

4.2 Experimental procedure

4.2.1 Overview of the experimental procedure

Once the experiment preparation procedure that was described in Chapter 2 was completed, the laser and cameras would be turned on for warming up. The TEC was started with a set temperature of 4°C. Also, the chamber pressure was maintained at an expected pressure value by adjusting the angle valve. When the convection pattern inside the cuvette became steady-state and the temperature of the TEC reached the set point, the cameras were started to collect images of the fluid motion near the water surface. The image recording process was followed by a temperature measurement using a thermocouple probe. Details on the experimental procedures including calibration of the camera, image recording and image processing are described in the following sub-sections.

4.2.2 Calibration of the CCD cameras

Calibration for the CCD cameras was performed for the following purposes; scaling of the cameras enables the recorded images to be shown and stored in scaled units representing the true dimensions; correcting the image distortion that was induced by perspective projection and inherent camera lens distortion; and lastly, obtaining the relation between the FOV of the two cameras which have a stereo alignment. A glass target (Microscope Calibration Plate, LaVision) which has equidistant distributed small dots on its surface was utilized for calibration.

Self-calibration was also carried out for the recorded images before image processing. It allows eliminating of the potential errors in the vector calculation due to misalignment of the calibration plate position and the laser sheet position. In a stereo-PIV

investigation, the two employed cameras should have identical FOV. In practice, discrepancy of the FOV would be induced due to imperfection of the optical alignment. This can be determined and corrected using the self-calibration function provided in a commercial code (Davis 7.2, LaVision 2007).

4.2.3 Image recording

In the experiment, the water surface was continuously receding within the cuvette due to evaporative mass transfer. The cameras were moved along with the water surface to keep the meniscus within the FOV. The FOV of the camera is illustrated in Fig. 2-3 and Fig. 4-1. Images of the convection field were recorded every 15 minutes over the course of 1 hour. A set of 100 images were captured each time at a frequency of 2Hz. The vapor-phase pressure within the vacuum chamber was also recorded simultaneous with the image recording.

Since the cuvette was placed in the vacuum chamber during the experiment, only the upper part of the cuvette was optically accessible from outside. When recording the first image set in each experiment, the height of the water within the cuvette was high enough for the camera to capture a second set of images while the FOV was vertically lowered by 5 mm. The second set of images was collected right after the first set of images. This was to extend the height of the FOV. The velocity fields calculated from these two image sets would be joined together after image processing. As water evaporated, the height of the water within the cuvette decreased because water was not continuously supplied to the cuvette. The height of the water that was optically accessible from outside was also decreased. Therefore, only at the beginning of the image recording were two sets of images collected rather than one.

4.2.4 Image processing

The collected raw images of the convection field have been processed using a commercial code (Davis 7.2, LaVision 2007). In the experiment, the laser sheet was non-uniformly distributed in the FOV of the camera because of the reflection of the tracer particles and refraction of the meniscus interface. Also, there was background noise on the collected images. Therefore, preprocessing steps were needed to improve the quality of the raw images before velocity vector calculation. They are 'subtracting sliding background' and 'subtracting offset' functions, to remove the background noise, and 'particle intensity normalization' function, to normalize intensities of the seeded particles. The 3-D velocity vectors were calculated by comparing consecutive 2-D views of the two cameras using a multi-pass stereo cross-correlation algorithm provided in the commercial code. The captured images were sub-divided into interrogation windows of 64×64 pixels for calculation. The velocity fields calculated from 100 images of each image set would be averaged.

Fig. 4-1(a) illustrates position and size of the FOV relative to the meniscus formed in the cuvette. A sample of calculated velocity field in 2-D views is shown in Fig. 4-1(b). As can be seen in the figure, the FOV of the cameras which is 8.88mm×6.71mm is covering most of the area of the meniscus. However, the area near the cuvette wall was not monitored because the cuvette is wider than the FOV. This is due to the restriction that the width of the overlap region of the two cameras is smaller than the width of the cuvette.

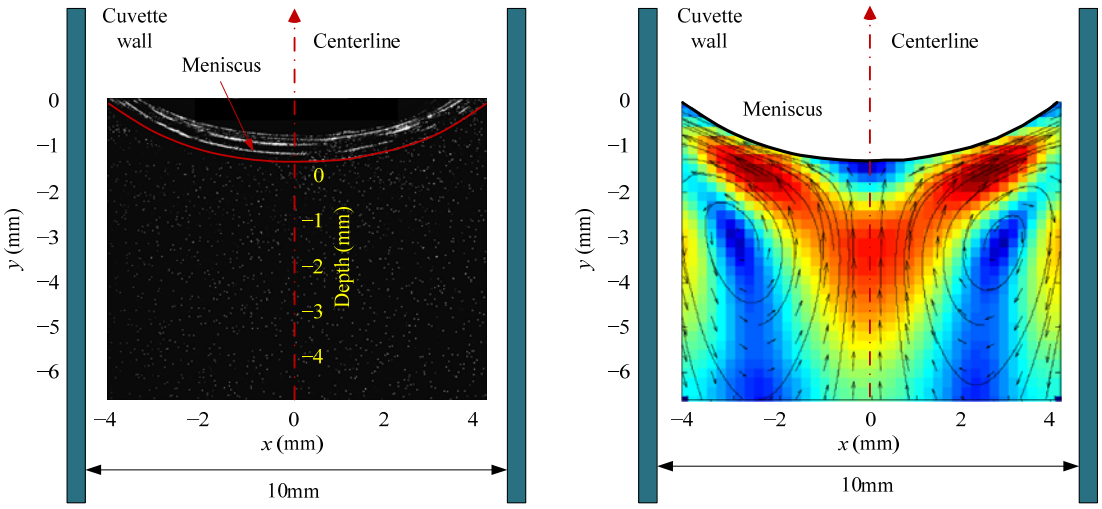

Figure 4-1. Schematic of a raw image (a) and a calculated velocity field (b)

4.3 Results

A convection roll was observed in the bulk water underneath its meniscus surface. Velocity and vorticity fields of the convection are shown in Fig. 4-2 and Fig. 4-3. Each of the velocity or vorticity field is an average of a set of 100 images. During the time period for recording the set of 100 images, the water surface moved less than 0.15mm and the displacement varied with the vapor-phase pressure. The position of the surface shown in these figures is the average position over the image recording period. Only the two-component velocity vectors on the *x*-*y* plane which was coincident with the laser sheet are demonstrated. The out-of-plane velocity vectors were near zero over the area of the FOV. This is because the laser sheet used as the illumination source passed through the cuvette in its central plane. According to the obtained velocity fields, the observed convection roll can be considered to be symmetric to the central plane of the cuvette. To examine the

repeatability of the evaporative convection roll, its velocity fields in 3 repeated experiments were compared. In addition, time dependence of the convection roll was investigated to ensure the convection was steady-state.

4.3.1 Velocity and vorticity fields of the observed convection

The calculated velocity and vorticity fields of the evaporative convection at different vapor-phase pressures are demonstrated in Fig. 4-2 and Fig. 4-3 respectively. As can be seen in Fig. 4-2, the convection patterns are similar to each other over the vapor-phase pressure range investigated. However, the strength of the convection decreases steadily as the pressure increases. The convection has two sections that are symmetric to each other with respect to the centerline of the cuvette. Water in each section rotates with the vorticity center in that section as shown in Fig. 4-3. In addition, the left upper part of the velocity field and vorticity field at a vapor-phase pressure of ~250 Pa are enlarged and demonstrated in Fig. 4-4 and Fig. 4-5 respectively.

The liquid water first accelerates along the meniscus interface from the center to the wedge, where the meniscus meets the wall of the cuvette. From there it moves back to the bulk water along the wall and returns to the center of the cuvette. It is then accelerated again while moving back to the meniscus interface. This can be seen in Fig. 4-6 which shows clearly how the velocity of the fluid changes against depth on the centerline of the cuvette. The velocity distributions on the centerline obtained at various vapor-phase pressures have similar profiles but different intensities. The overall flow velocity increases as the vapor-phase pressure decreases. On the centerline of the cuvette, the water flow accelerates slightly from the bottom of the FOV to ~5 mm beneath the water surface which indicates the central point of the meniscus interface in this case. From

there the flow velocity starts to increase dramatically and peaks at ~2 mm below the meniscus interface. The flow then decelerates significantly until it reaches the surface where it becomes quiescent.

An interesting phenomenon that needs to be mentioned is change of the convection pattern when the vapor-phase pressure was increased to ~820 Pa. Different from the other convections that are shown above, only the upper part of the water is rotating with the two vorticity centers that are near the water surface. The lower part of the fluid is rotating in an opposite direction. This can also be seen in Fig. 4-6. The water flow moves upward at a level higher than the depth of ~6 mm, but turns downward for the lower region of the cuvette. These results lead to the hypothesis that size of the convection roll decreases as a consequence of increasing of the vapor-phase pressure. However, this was not examined for pressures higher than 820 Pa.

To investigate how the evaporation process would affect the strength of the observed convection, the mean evaporation rate of the water at various vapor-phase pressures was investigated and demonstrated in Fig. 4-7. The mean evaporation rate is defined as the ratio of the average mass transfer rate to the area of the meniscus surface. Since the meniscus surface formed in the rectangular cuvette was considerably complicated, it was calculated approximately by multiplying the length of two meniscus arc obtained from two perpendicular side views.

As shown in the figure, the mean evaporation rate increases steadily as the pressure decreases. Its varying trend against vapor-phase pressure is consistent with that of the strength of the convection as shown in Fig. 4-2, Fig. 4-3 and Fig. 4-6. This indicates that increase of the evaporation flux can enhance the strength of the convection.

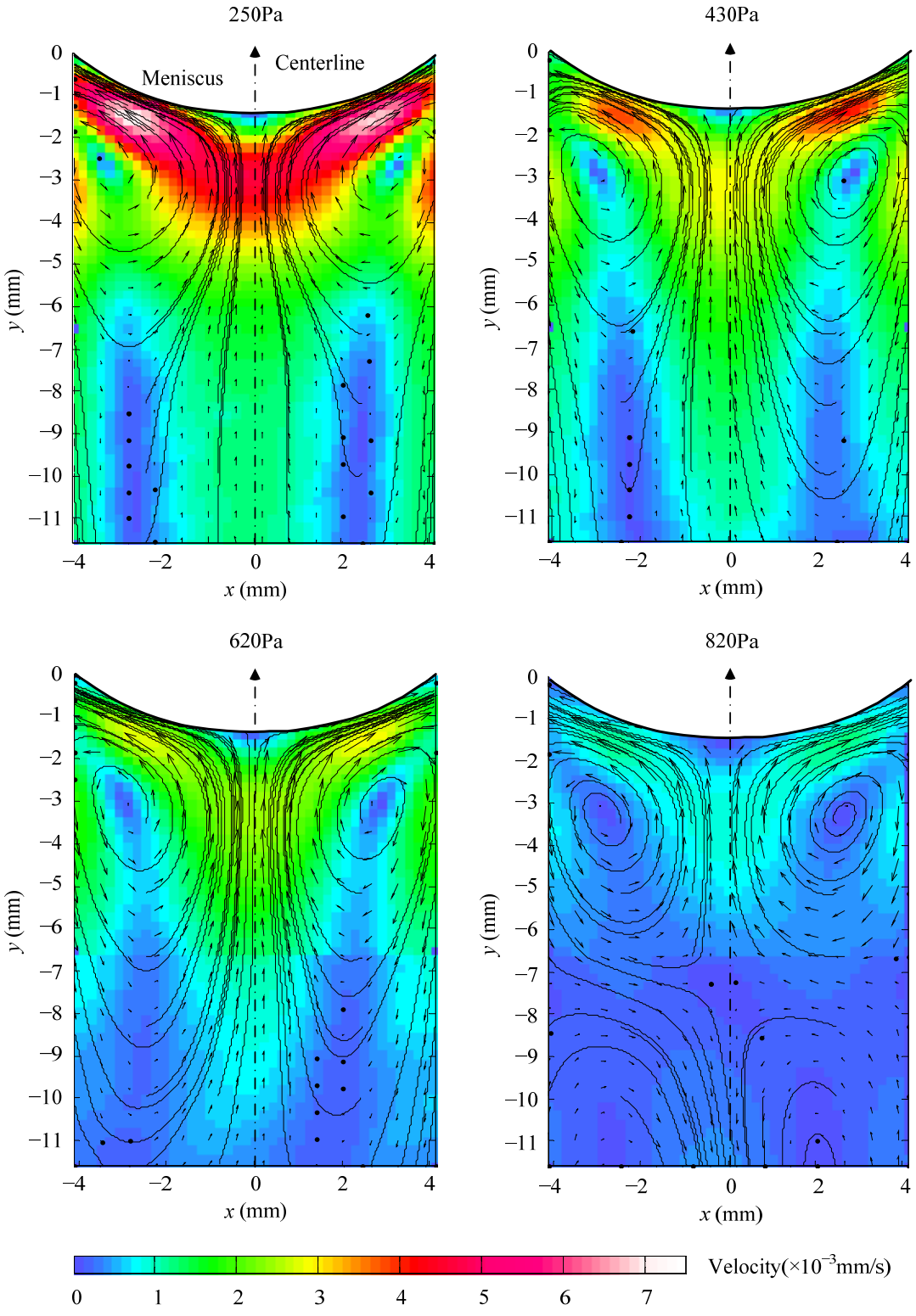

Figure 4-2. Velocity fields of the observed convection at various vapor-phase pressures

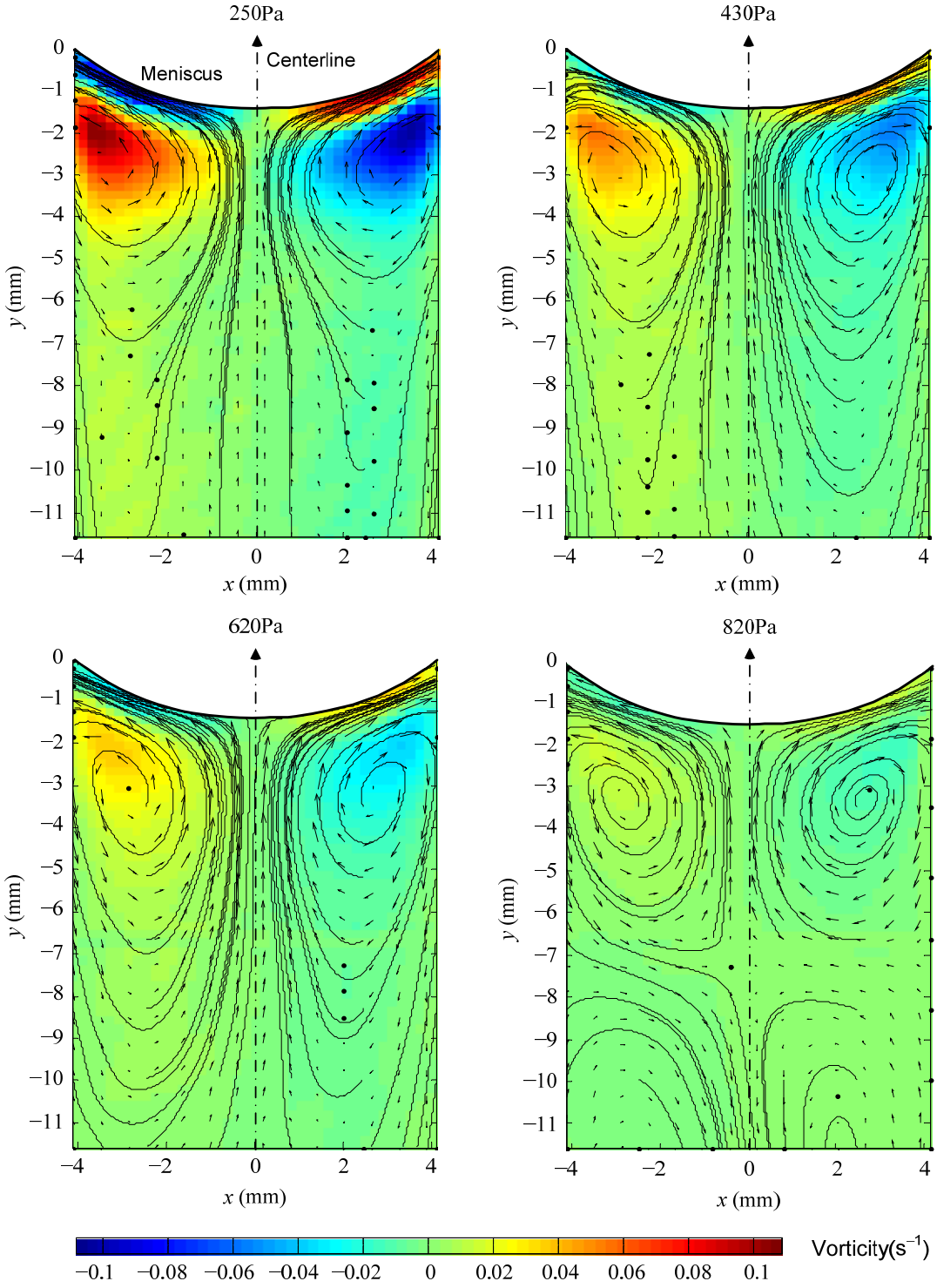

Figure 4-3. Vorticity fields of the observed convection at various vapor-phase pressures

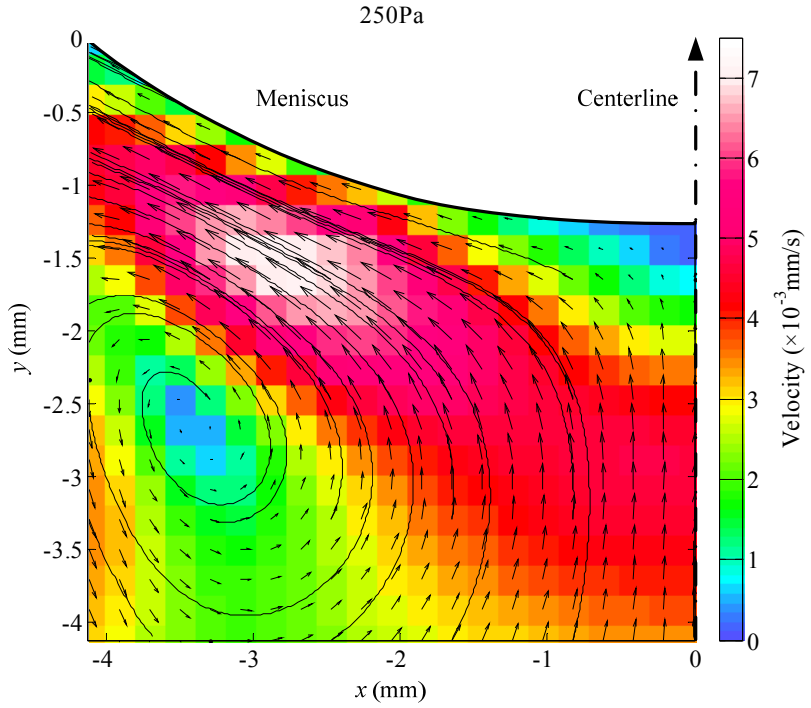

Figure 4-4. Enlarged velocity field for the case of 250 Pa vapor-phase pressure

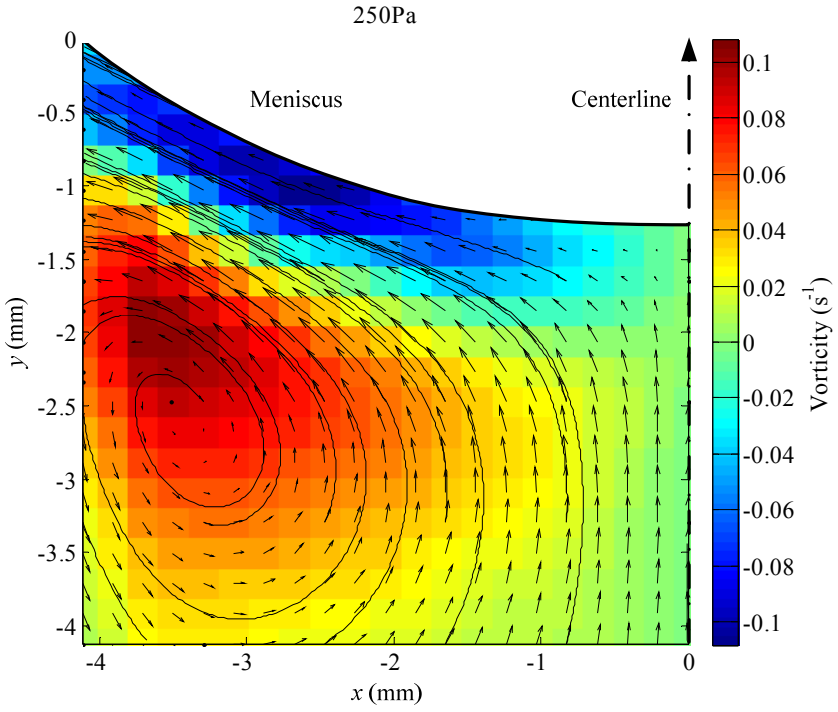

Figure 4-5. Enlarged vorticity field for the case of 250 Pa vapor-phase pressure

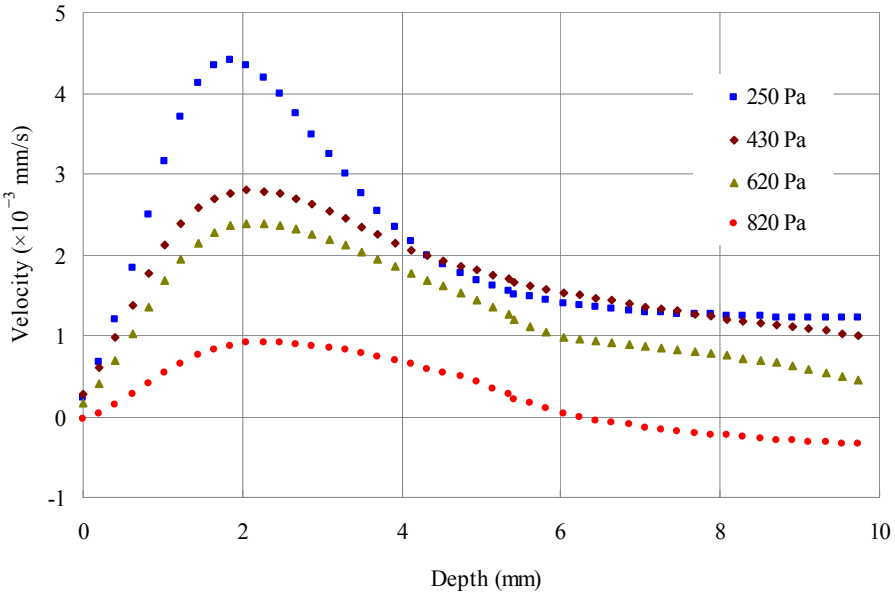

Figure 4-6. Velocity distribution on the centerline of the cuvette at different vapor-phase pressures

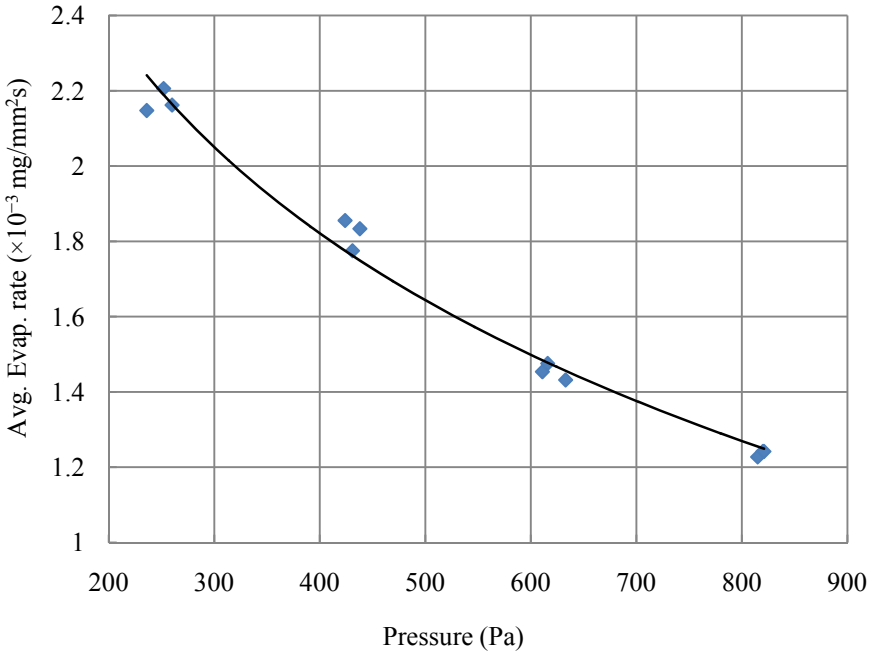

Figure 4-7. The relation between the average evaporation rate of the water and the vapor-phase pressure

4.3.2 Repeatability and time dependence of the observed convection

To ensure the experimental results are precise, repeatability and time dependence of the convection roll were both examined for the condition of 430 Pa vapor-phase pressure. Fig. 4-8 shows the velocity fields of the convection in the three repeated experiments. They are averaged velocity fields calculated from 100 images of the first collected image sets in each experiment. Fig. 4-9 describes the corresponding velocity distribution on the centerline of the cuvette. The figures show that the convection patterns are similar while there are slight differences in intensity of the velocity fields which can be attributed to experimental error.

Change of the convection over time can be seen in Fig. 4-10, which shows the velocity fields of the convection at 15 minutes intervals in the same experiment. They are averaged over 100 velocity fields. Although the water surface dropped 2.3 mm every 15 minutes, the cameras were moved along with the water surface to keep the meniscus within the FOV. Therefore, the FOV always covers the same area of the convection. Fig. 4-11 shows the corresponding velocity profiles on the centerline of the cuvette. Over the course of 45 minutes, the convection pattern remains steady. However, the velocity distribution curve on the centerline varies by ~10%. This variation over time is comparable to the difference between repeated experiments.

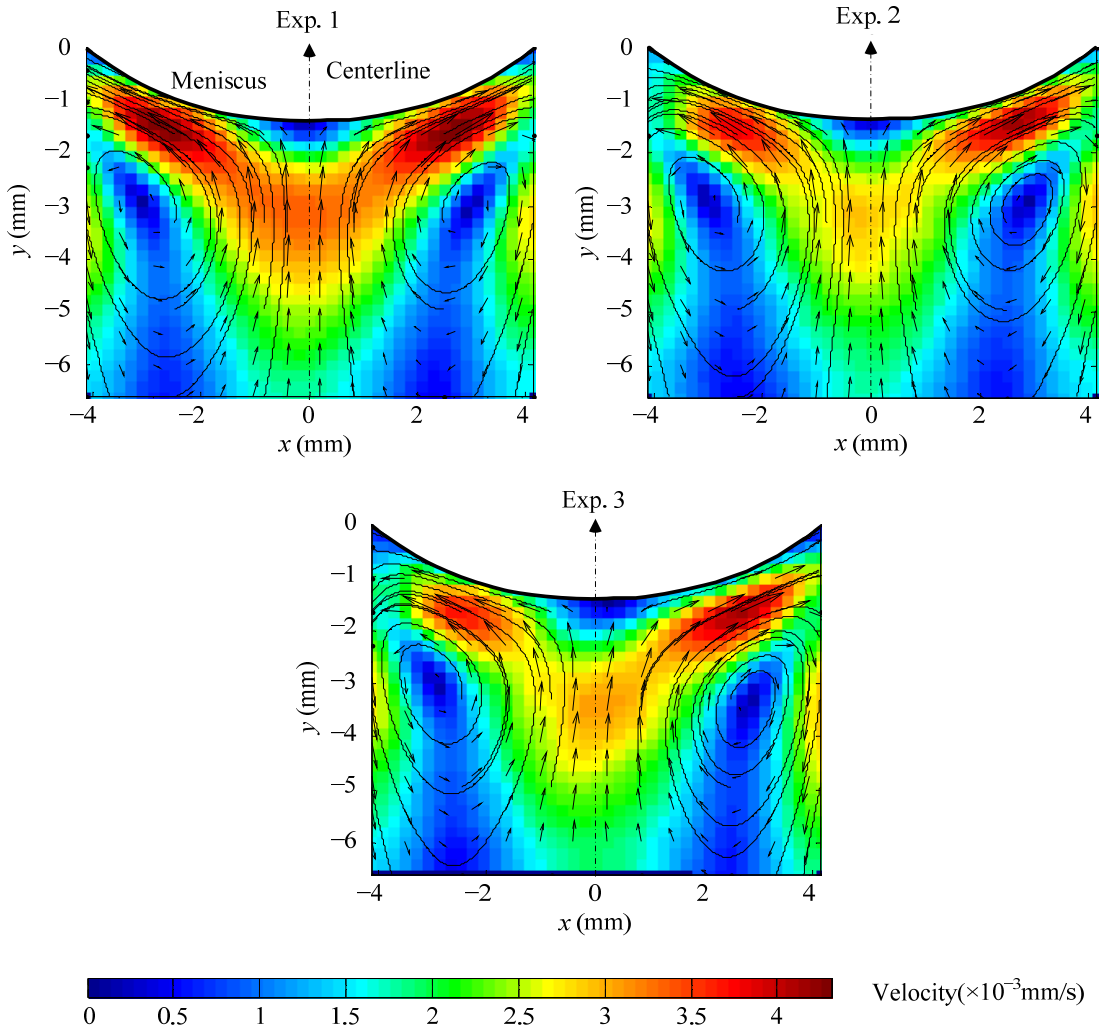

Figure 4-8. Velocity fields of the convection for 3 repeated experiments

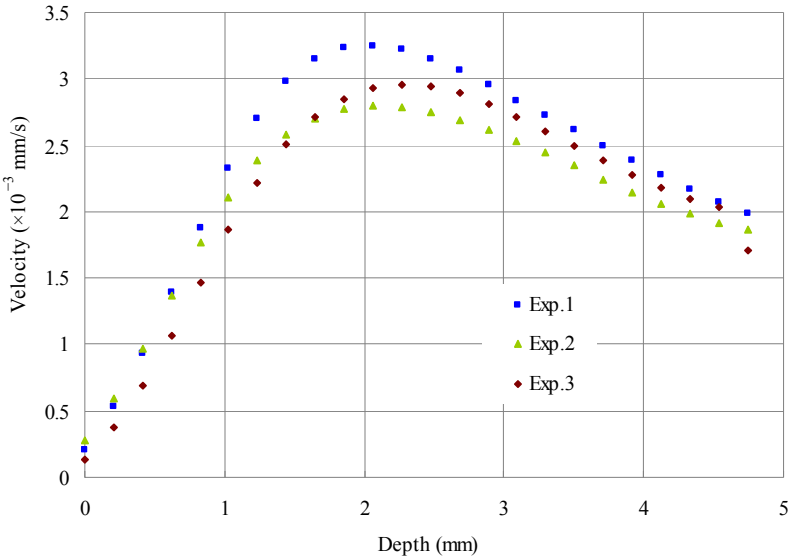

Figure 4-9. Velocity distribution on the centerline of the cuvette in the 3 repeated experiments

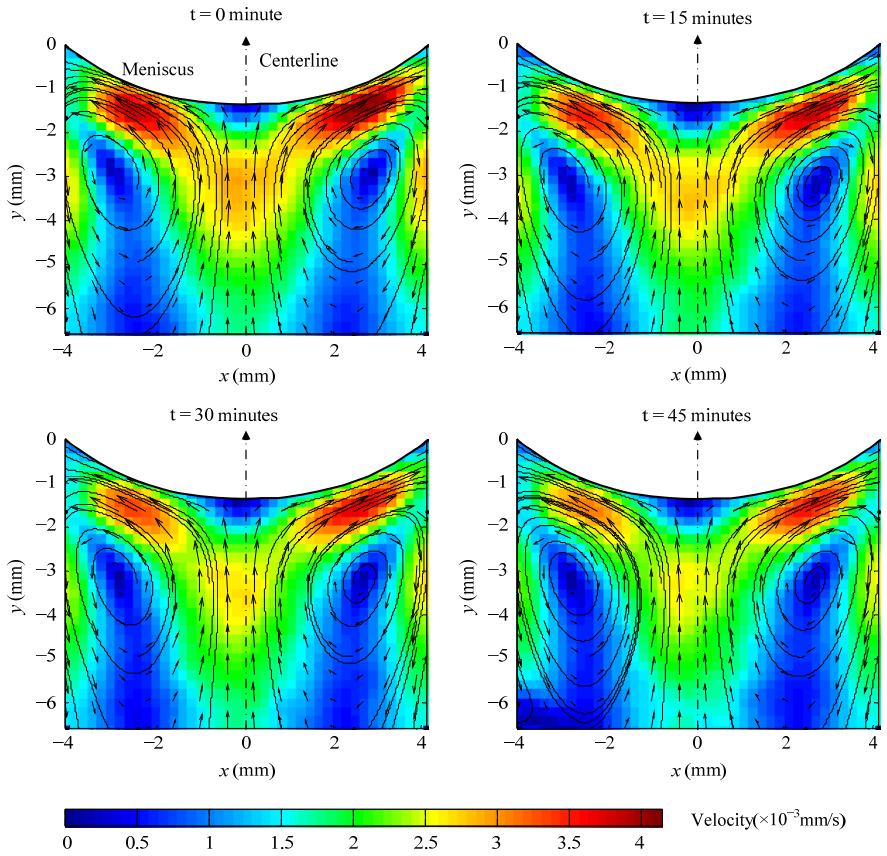

Figure 4-10. Velocity fields of the convection at 15 minutes intervals at a system pressure of 430 Pa

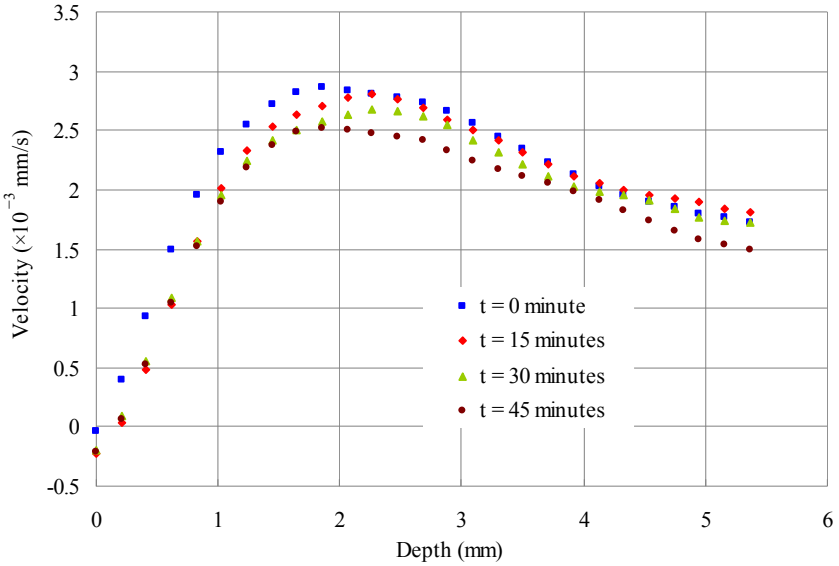

Figure 4-11. Velocity distribution on the centerline of the cuvette at 15 minutes intervals at a system pressure of 430 Pa

4.4 Discussion and conclusion

When water was evaporating within the vacuum chamber, the convection roll that was adjacent to the water meniscus surface was observed. This indicates that the energy transfer in the bulk water for the evaporation process was through conduction and convection. As the evaporation rate increased by reducing the vapor-phase pressure, the velocity of the convection roll was also increased. This revealed that evaporation played an important role for generating the convection.

As described in Chapter 3, the temperature measurement using thermocouple demonstrated that the column of water was density stabilized along the centerline of the cuvette. However, the 2-D density distribution over the convection field was still not clear. Therefore, the convection could be driven by either surface tension or buoyancy. In

order to determine the driving mechanism of the convection, a 2-D temperature measurement needs to be performed.

CHAPTER 5 : STUDY OF THE TWO-DIMENSIONAL TEMPERATURE PROFILE OF MARANGONI CONVECTION BY PLIF

Evaporative convection of water in a vacuum chamber was observed and described in Chapter 4. It was visualized and characterized by applying the stereo-PIV. The convection was also found to be repeatable in different experiments that have the same experimental conditions. However, the temperature profile of the flow field was still needed to determine the driving mechanism of the convection. Therefore, the two-color/two-dye PLIF technique was applied to investigate the 2-D temperature distribution over the flow field. The same experimental setup, conditions and procedure were followed to ensure that the obtained convection would be the same as that observed in the stereo-PIV investigation.

5.1 Experiment conditions

The PLIF investigation was performed only for a single condition that has a vapor-phase pressure of 430±15 Pa. It was repeated 3 times to examine the repeatability of the results. In order to control the temperature profile of the water within the cuvette, the temperature of the TEC was kept at 4°C when it was running in the experiments. The

experimental setups for the study were shown in Fig. 2-2 to Fig. 2-5 and were described in Chapter 2.

5.2 Fluorescence characteristics

5.2.1 Selection of fluorescent dyes

Two fluorescent dyes are required for a two-color PLIF investigation. One of them should be strongly temperature-dependent to sense the temperature, while the other one should be non-temperature-dependent to indicate the concentration of the fluorescent dye. They should have similar absorption spectra, which allows them to be excited by the same laser source, but quite different emission spectra, so that their emission light can be split up easily.

RhB and Rh110 are the most popular fluorescent dyes for two-color PLIF. They have been utilized as the temperature-sensitive dye and the non-temperature-sensitive dye respectively in many studies [32, 34 and 35]. RhB is usually used as the temperature-sensitive dye because of its strong temperature sensitivity which is as high as 2.3% $°C^{-1}$ [32]. In contrast, Rh110, whose temperature sensitivity is as low as 0.13% $°C^{-1}$ [32], is used as the corresponding non-temperature-sensitive dye. The absorption and emission spectra of RhB and Rh110 are revealed in Fig. 5-1. It can be seen that their absorption spectra overlap each other over a wide range while their emission spectra are ~50 nm apart. This spectral property of RhB and Rh110 make them suitable for fluorescent dyes of a two-color/two-dye PLIF investigation. They were therefore selected in this study.

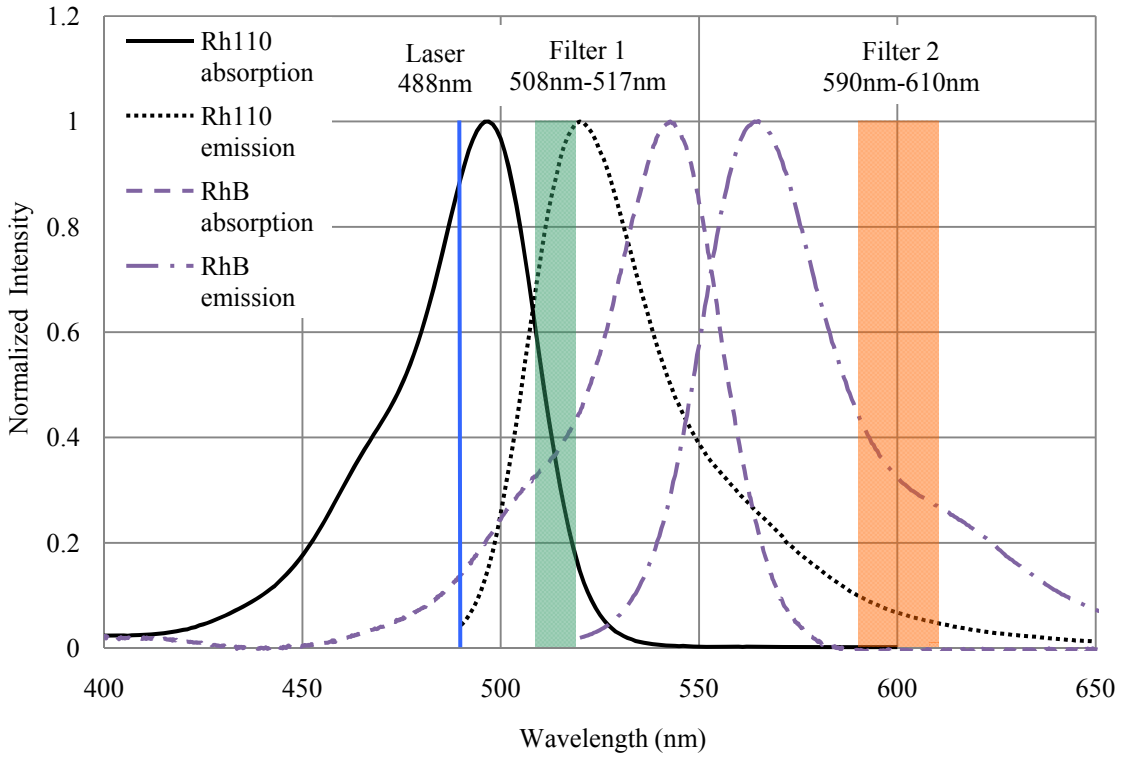

Figure 5-1. Absorption and emission spectra of Rh B and Rh 110

5.2.2 Spectral characteristics

To excite the two fluorescent dyes at the same time, the exciting light wavelength should be in the overlapping range of the absorption spectral bands of RhB and Rh110. In addition, in order to eliminate the scattering light when collecting emission light from the objective volume, the exciting light should be able to be separated from the emission light.

In this study, an Argon-ion laser that has a wavelength of 488 nm which is shown by the blue line in Fig. 5-1 was chosen as the laser source. In order to separate the emission light fluoresced by the two fluorescent dyes, two bandpass light filters with different wavelength ranges were utilized to selectively transmit light according to its

wavelength. Only the light in the wavelength range can go through the light filter, and the out-of-range light would be cut off. One of the selected light filters which has a wavelength range of 508 nm to 517 nm was used for extracting emission light of Rh110 whose emission peak is at 520 nm. Its wavelength range is indicated by the green shadow in Fig. 5-1. As can be seen in the figure, there is no emission light of RhB distributed in this wavelength range, which ensures that transmitted light from this filter would be purely fluoresced by Rh110. The other light filter that has a wavelength range of 590 nm to 610 nm was selected for RhB. Its wavelength range is illustrated by the orange shadow in Fig. 5-1. In this spectral band, the emission light intensity of RhB is much stronger compared with the emission light intensity of Rh110. This allows the transmitted light from this light filter to be considered as emitted from RhB only, and the noise signal emitted by Rh110 can be neglected.

5.2.3 Temperature dependence

In order to implement a two-color/two-dye PLIF temperature measurement, a calibration curve between temperature and fluorescence intensity ratio of the two dyes is necessary. In a calibration experiment, the calibration curve can be obtained by collecting both the fluorescence intensities and the corresponding local temperature of the dye solution at the same time while changing the temperature over a proper range. The temperature of the dye solution has to be maintained spatially constant [32, 33, 35 and 36]. In this way the local temperature that is corresponding to the collected fluorescence intensities can be determined easily and accurately. In contrast, if the temperature distribution in the dye solution is not uniform, the collected fluorescence images would

also be non-uniform. As a result, the relation between fluorescence intensity and temperature would be difficult to determine.

In the actual PLIF experiment of this study, the water to be investigated could have a temperature of sub-0°C but remain in liquid-phase while it's evaporating at a high evaporation rate within the vacuum chamber. In this evaporation process, the temperature distribution in the bulk water varies due to the evaporation effect. This is displayed in Fig. 3-2 which shows temperature profile from the thermocouple measurements on the centerline of the cuvette. In order to execute a calibration experiment over the similar temperature range, water needs to be cooled to a temperature of subzero while it remains in liquid-phase. This can be satisfied by letting the water evaporates in its own vapor at a low vapor-phase pressure within the vacuum chamber. However, as described before, the temperature distribution in the bulk water won't be uniform, which leads to a difficulty in correlating the fluorescence intensity with temperature. In addition, if water is exposed to atmospheric pressure, it would be frozen when its temperature is below zero. Due to these constraints, a typical calibration experiment that has been used in previous studies [32, 34 and 35] was not used in this study.

To overcome this problem, a different calibration method was proposed. That is, instead of performing a calibration experiment prior to the actual experiment, the fluorescence images collected in the actual experiment were calibrated versus the temperature values measured by the thermocouple. This method is based on the two findings that the temperature profile of the water within the cuvette is repeatable in different experiments that have the same experimental conditions, and also, that the fluorescence intensity ratio gradient reflects temperature gradient.

The former finding is described in Chapter 3. That is, for the same vapor-phase pressure, the temperature profile on the centerline of the cuvette is repeatable in different experiments. This should also apply for the PLIF experiment, because what differ the PLIF experiment from the stereo-PIV experiment is nothing but the measurement technique. Therefore, the temperature profile measured by the thermocouple is also valid for the PLIF experiment. As can be seen in Fig. 3-3, when the vapor-phase pressure within the vacuum chamber was at ~430 Pa, the temperature profile on the centerline is nearly linear.

The later finding can be seen in Fig. 5-2, which demonstrated how the fluorescence intensities of RhB and Rh110 vary against temperature. It was studied by Sakakibara and Adrian [32] in their investigation of a PLIF temperature measurement. The fluorescence intensity is normalized by its value at a temperature of 20°C. Over the temperature range of 15°C to 40°C, the intensity change of RhB is dramatic, and the varying trend can be approximately considered as linear. In contrast, the fluorescence intensity of Rh110 remains nearly constant over the temperature range. As a result, varying trend of the fluorescence intensity ratio of RhB and Rh110 would also be expected to be linear.

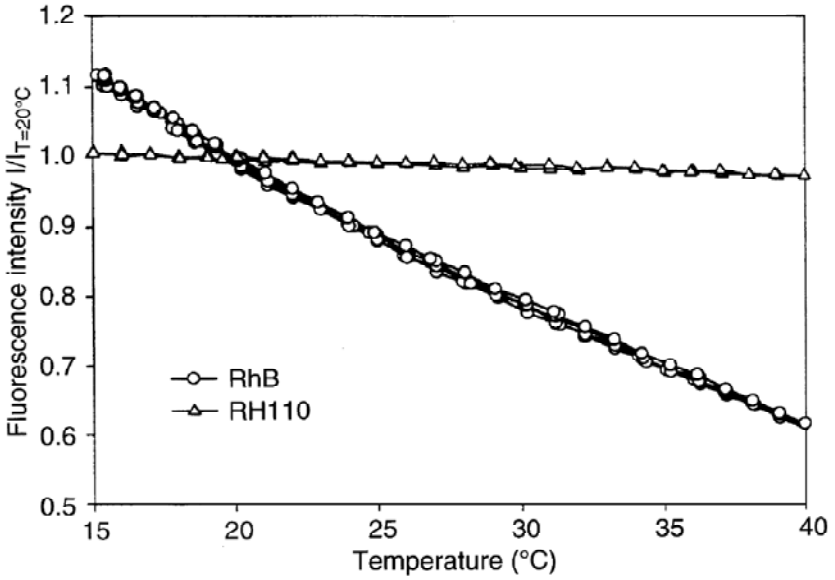

Figure 5-2. Variation of fluorescence intensities of RhB and Rh110 against temperature [32]

In order to calibrate the fluorescence images versus temperature, the fluorescence intensity ratio on the centerline of the cuvette needs to be known. After the fluorescence images were collected and processed, a ratio image would be calculated by dividing the fluorescence intensity of RhB by the fluorescence intensity of Rh110. The intensity ratio profile on the centerline can then be extracted by averaging the ratio over a 0.2 mm (30 pixels) wide band at the center of the ratio image. Fig. 5-3 illustrates the obtained fluorescence intensity ratio profiles for three different experiments at the same vapor-phase pressure of 430 Pa. They are averaged over 100 PLIF images. The fluorescence intensity ratio curves are in reasonable agreement with each other although there is a slight disagreement between them. They can all be fitted with linear lines. This is what is to be expected because both the temperature profile on the centerline and the temperature dependence of the fluorescence intensity ratio are linear.

The section between the water surface and 1 mm below is not displayed because the signal is too noisy. This is because the intensity of the laser sheet used in the experiment fluctuated significantly near the water surface, and any small misalignment of the two dyes' fluorescence images could result in large errors when calculating the intensity ratio. The fluctuation of the intensity near the top of the laser sheet is induced by a knife edge that was used to block the upper part of the laser sheet.

Fig. 5-4 shows the calibrated temperature profiles and the temperature profile measured by thermocouple on the centerline of the cuvette. The completed thermocouple results are showed in Fig. 3-2. As can be seen in Fig. 5-4, the temperature profiles are in decent agreement with each other. The fluorescence intensity ratio was calibrated in a temperature range of ~-0.3°C to ~-1.8°C. However, the calibration curve was also used for temperature out of this range. This is reasonable because the calibration curve can be approximately regarded as linear.

5.3 Experimental procedure

5.3.1 Experimental apparatus operation

Once the experimental preparation procedure that was described in section 2.3 was completed, the laser and cameras were turned on to warm up. The TEC was started with a set temperature of 4°C. At the same time, the vapor-phase pressure was changed to ~430 Pa by adjusting the angle valve. When the convection pattern within the cuvette became steady-state and the temperature of the TEC reached 4°C, the cameras would be started to collect measurement images.

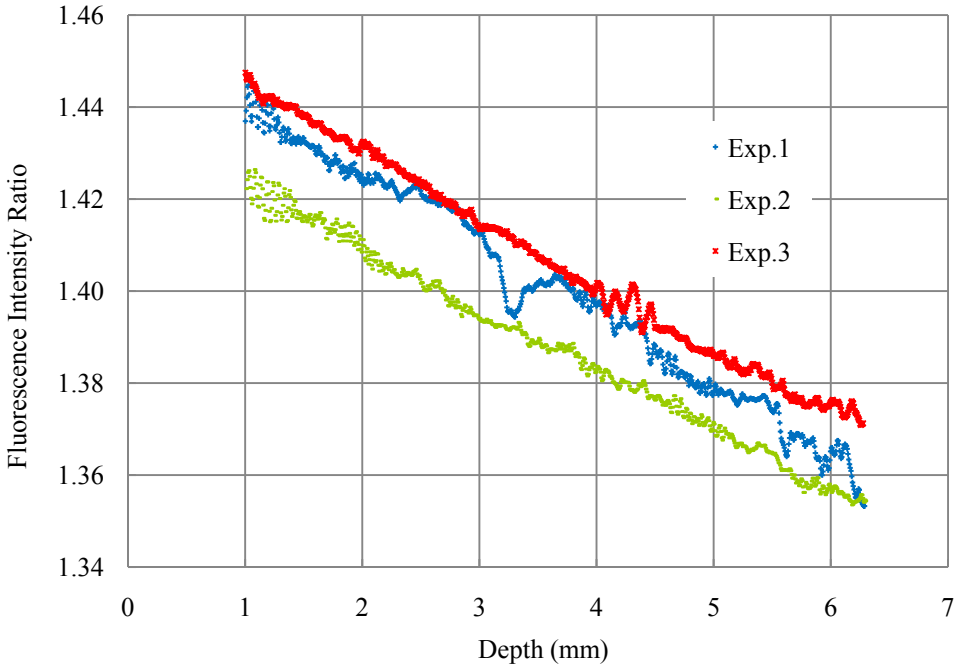

Figure 5-3. Fluorescence intensity ratio on the centerline of the cuvette at a vapor-phase pressure of ~430 Pa

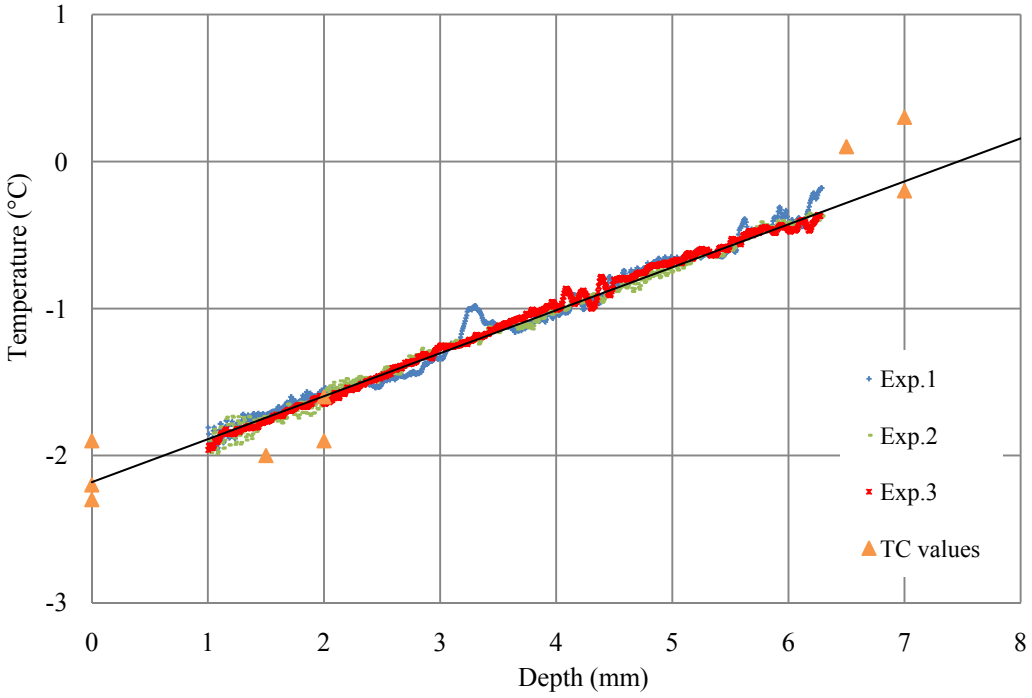

Figure 5-4. Calibrated temperature profile on the centerline of the cuvette and the temperature profile measured by thermocouple

5.3.2 PLIF measurement

The workflow of the PLIF measurement is described in Fig. 5-5. It consists of image recording, image processing and intensity calibration. The intensity calibration method was described in section 5.2.3. The rest will be explained in detail in the following sub-sections.

5.3.2.1 Calibration of the CCD cameras

Calibration for the CCD cameras has to be performed before each experiment for the following purposes: scaling of the cameras, which enables the recorded images to be shown and stored in scaled units representing the true dimensions; correcting the image distortion that was induced by perspective projection and inherent camera lens distortion; and lastly, obtaining the relation between the FOV of the two cameras which have a stereo alignment. This is important for calculating the fluorescence intensity ratio of the two dyes. A glass target (Microscope Calibration Plate, LaVision) which has equidistant distributed small dots on its surface was utilized for calibration.

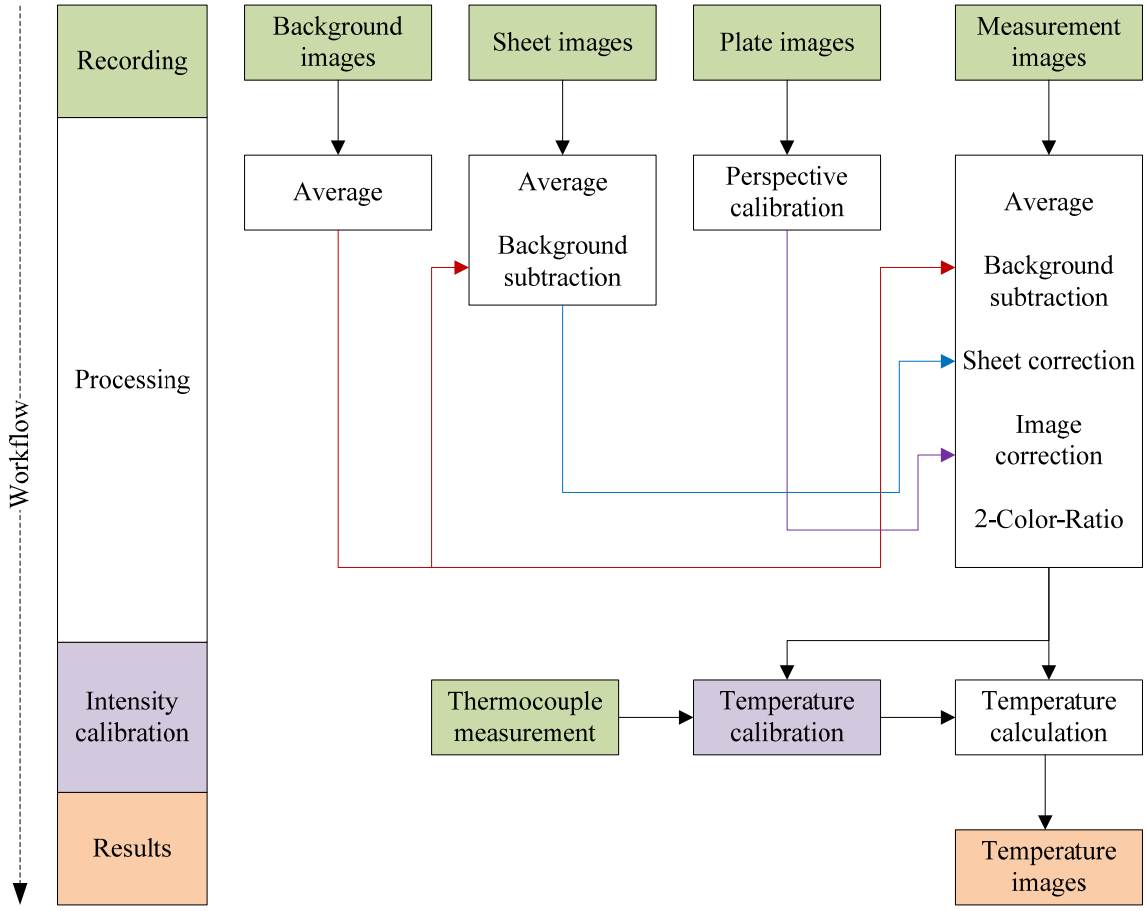

Figure 5-5. Workflow of the temperature measurement procedure of PLIF

5.3.2.2 Image recording

Before recording experiment images, background images and sheet images need to be captured with the same exposure time as the experiment images, they will be used for correcting the experiment images in the image processing process.

Each experiment image includes not only the PLIF signal but also a background signal, which is from the camera's dark current and potentially from surrounding scattered light. The background signal must be recorded and subtracted from the experiment images before image processing. Since two bandpass light filters were used

and they can eliminate scattered light, noise induced by the camera's dark current would be the dominant source of the background signal. Therefore, the background images can be recorded with the camera lens closed. A set of 50 background images were recorded continuously in each experiment. They would be averaged before use.

Sheet images also need to be captured to eliminate inaccuracy of the experimental images induced by nonuniformity of the laser sheet intensity and local variations of the optical transmission. When recording the sheet images, the experimental setup has to be the same as in the actual experiment. Besides, the experimental solution needs to have uniform temperature and homogeneous dye concentration. In each experiment, a set of 50 sheet images were recorded for sheet correction.

In this investigation, the utilized laser sheet was fixed and below the water-vapor interface when it is set up. Therefore, in order to record the fluorescence images of the area right beneath the meniscus surface without intersecting with the meniscus to avoid refracting light, the images were captured when the meniscus was about to contact with the top edge of the laser sheet. The FOV when collecting images are shown in Fig. 5-6. The measurement images were recorded for a set of 20 at a frequency of 0.9Hz while the exposure time was 1s. The number of images was smaller than the background images and sheet images. This is to reduce the image recording time, because during the recording process, the water surface was dropping and therefore changing the temperature distribution in the laser sheet area.

5.3.2.3 Image processing

Image processing was performed by using the commercial code (Davis 7.2, LaVision 2007). The processing procedure is detailed in Fig. 5-5. As can be seen in the

figure, the measurement images were averaged first to reduce noise, followed by background subtraction and sheet correction to improve the accuracy. Image correction was executed after to correct image distortion. After these processing steps, the corrected measurement images would be ready for calculating the 2-color-ratio images which represent the temperature distribution. At the end, a temperature calculation function would be used to transfer the intensity ratio images to temperature maps by applying the obtained calibration curve. Fig. 5-6 demonstrated raw fluorescence images of RhB and Rh110 and the calculated temperature map.

5.4 Results and error analysis

5.4.1 Results

Temperature maps obtained from the three repeated PLIF measurements at a vapor-phase pressure of ~430 Pa are demonstrated in Fig. 5-7, Fig. 5-9 and Fig. 5-11. As shown in the figures, the temperature maps have the same symmetric pattern and fairly close temperature distributions. The temperature maps can be divided into three regions; a bottle-neck shaped middle region, and the two side regions that are separated by the middle region. The horizontal temperature profiles at a depth of 1 mm, 3 mm and 5 mm in the liquid water for the three experiments are also plotted in Fig. 5-8, Fig. 5-10 and Fig. 5-12 respectively. It can be seen that, in the three repeated experiments, the temperature profiles are consistent with each other in the middle region but differ significantly in the side regions.

It can be seen in Fig. 5-8, Fig. 5-10 and Fig. 5-12 that the temperature profiles for different experiments and different depths are nearly symmetric with respect to the centerline. However, the temperature of the right side, from where the laser enters the

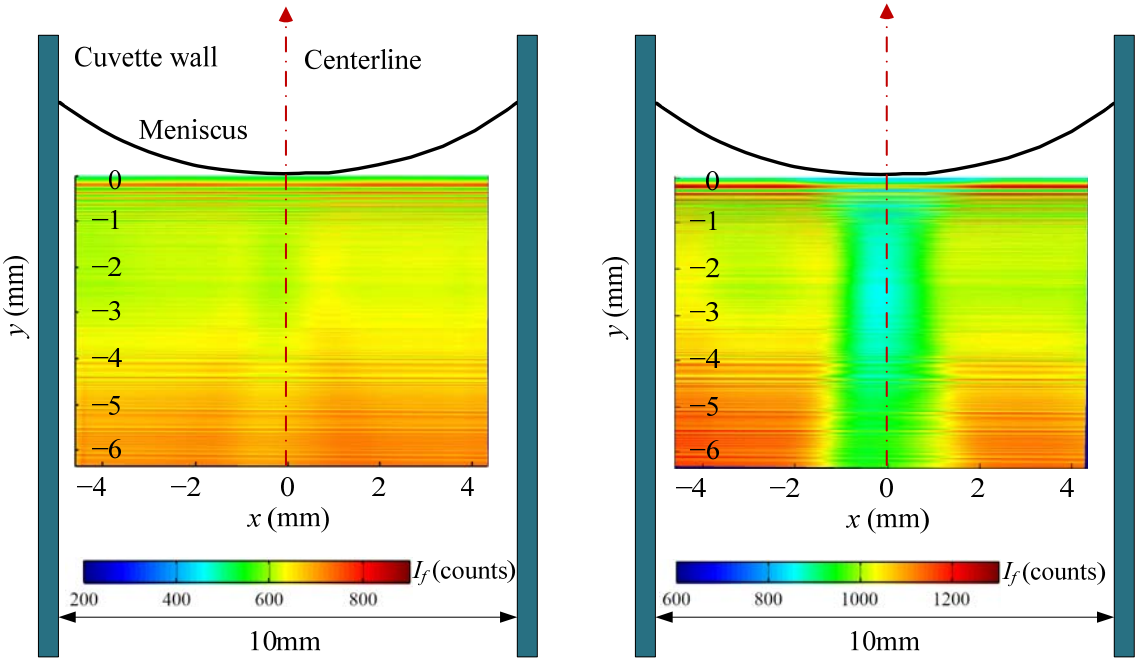

(a) Fluorescence image of Rh110

(b) Fluorescence image of RhB

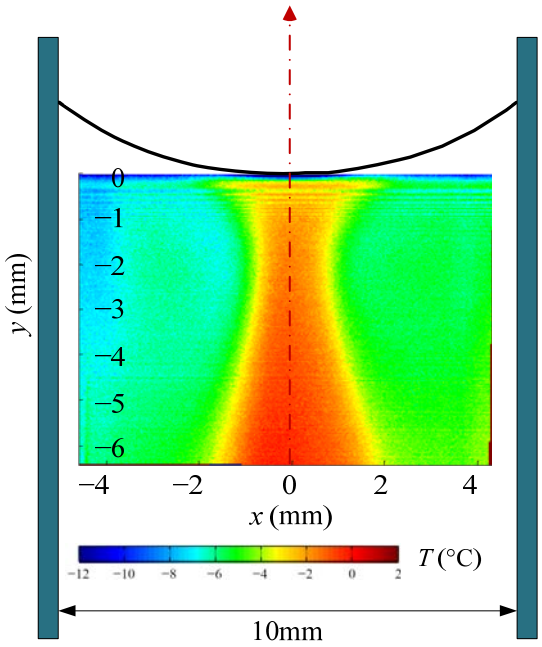

(c) Calculated temperature map

Figure 5-6. Raw fluorescence images of RhB and Rh110 and calculated temperature map

liquid water, is always slightly higher than the temperature of the left side. The temperature difference can reach as much as ~2°C. Theoretically, these temperature profiles should be exactly symmetric about the centerline, therefore, the temperature difference between the two sides can be considered as experimental error that was induced mostly by the laser sheet attenuation while propagating in the liquid water.

In the middle region, the temperature is higher at the centerline and decreases when departing from the centerline. On the centerline of the cuvette which is also the centerline of the middle region, the temperature decreases linearly from the bottom of the FOV to the water-vapor interface as also shown in Fig. 5-4.

In contrast, the temperature distributions in the side regions are more invariable but fluctuating. The temperature distribution within the two regions does not change dramatically. It slightly decreases with height but basically keeps constant horizontally, although fluctuating significantly.

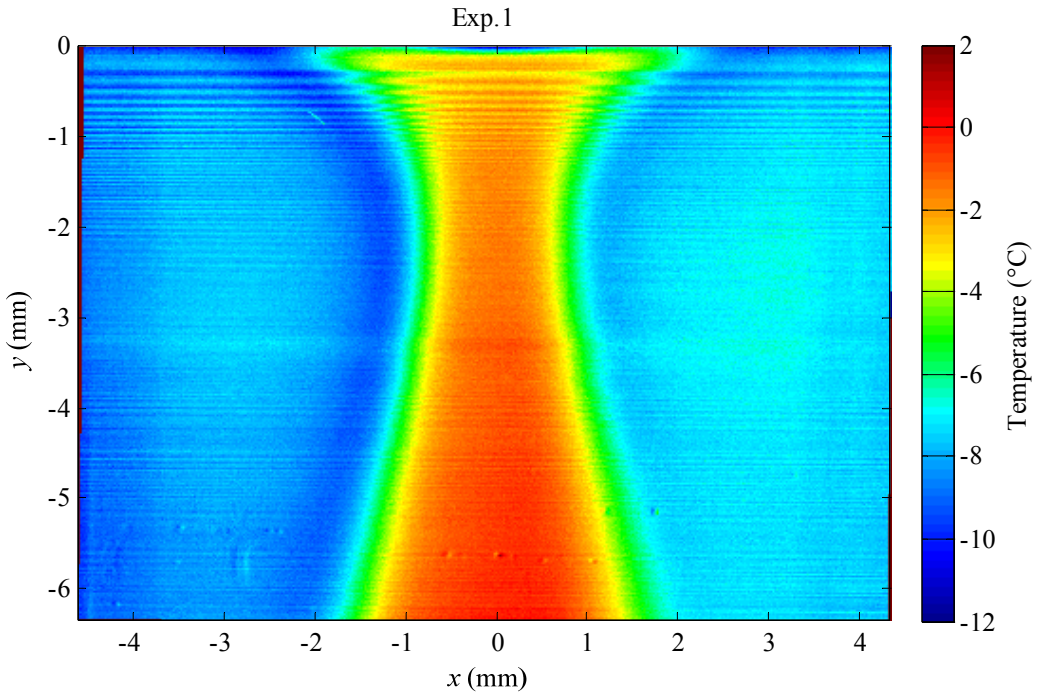

Figure 5-7. 2-D temperature profile of the convection field observed in experiment 1

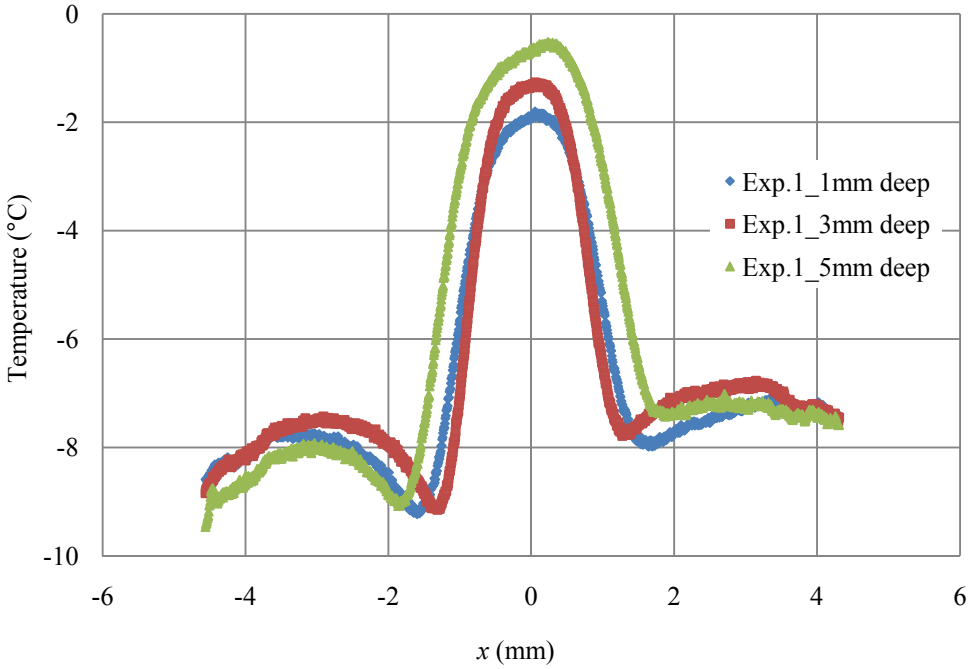

Figure 5-8. Horizontal temperature profile at a depth of 1 mm, 3 mm and 5 mm in the bulk water in experiment 1

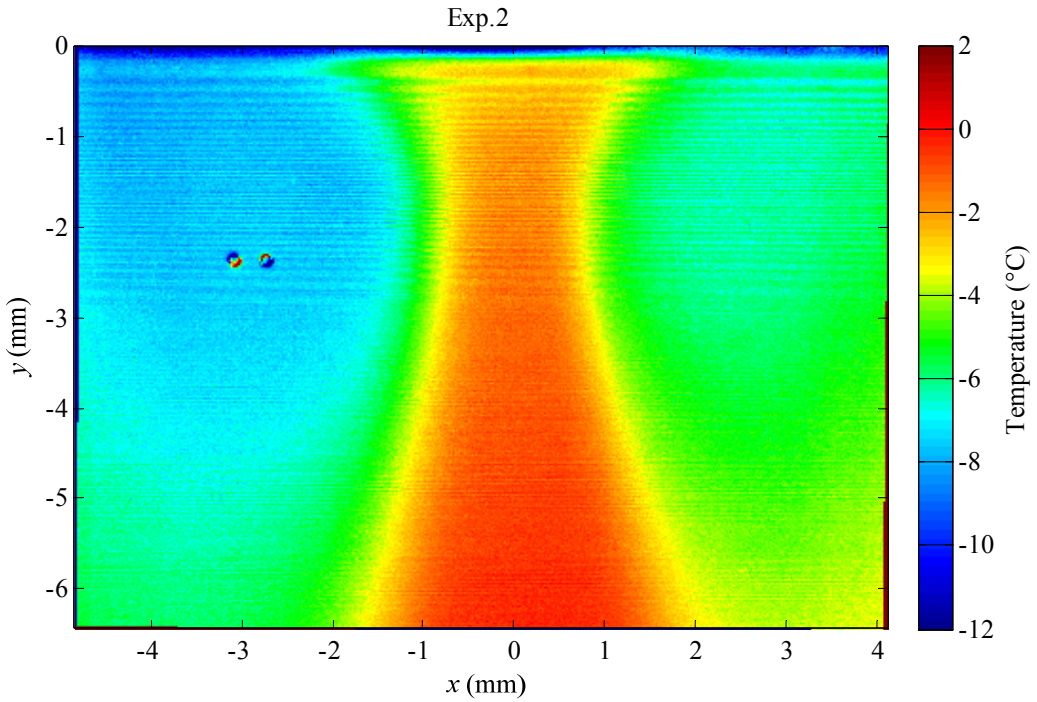

Figure 5-9. 2-D temperature profile of the convection field observed in experiment 2

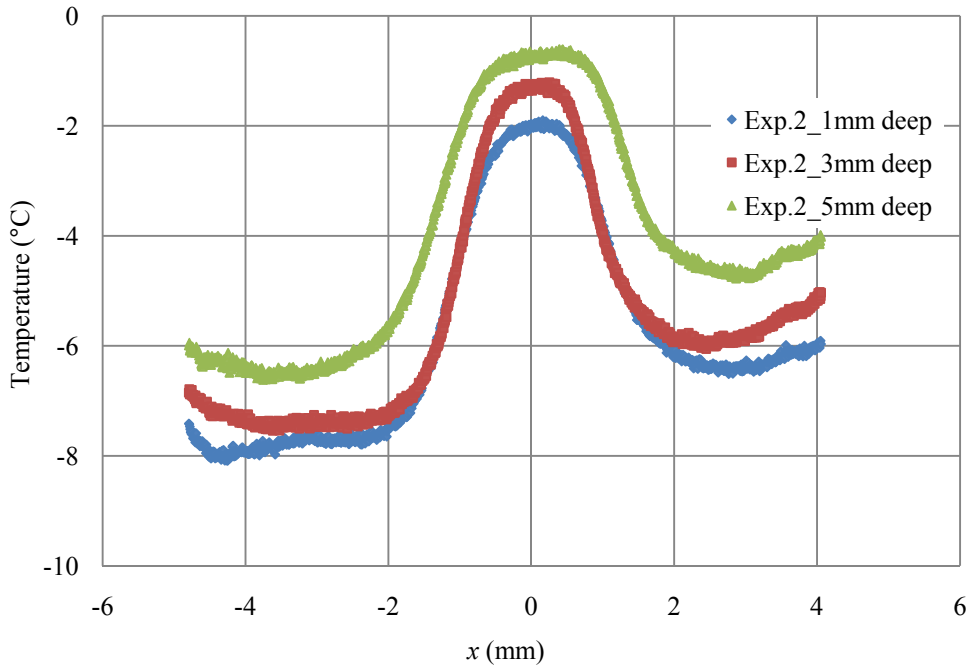

Figure 5-10. Horizontal temperature profile at a depth of 1 mm, 3 mm and 5 mm in the bulk water in experiment 2

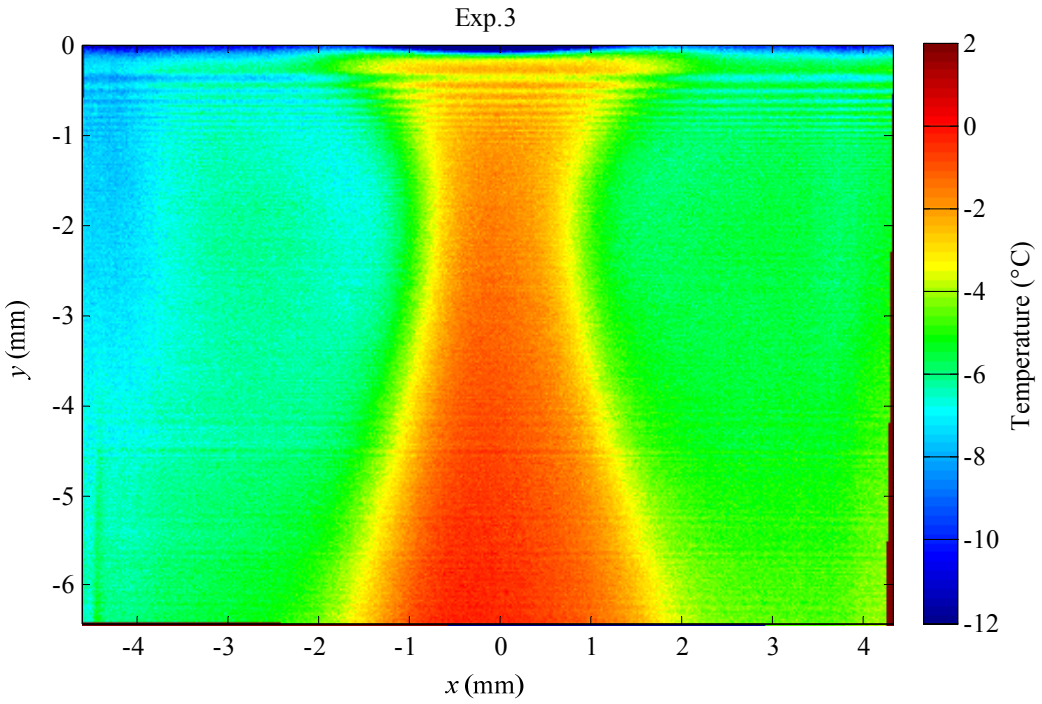

Figure 5-11. 2-D temperature profile of the convection field observed in experiment 3

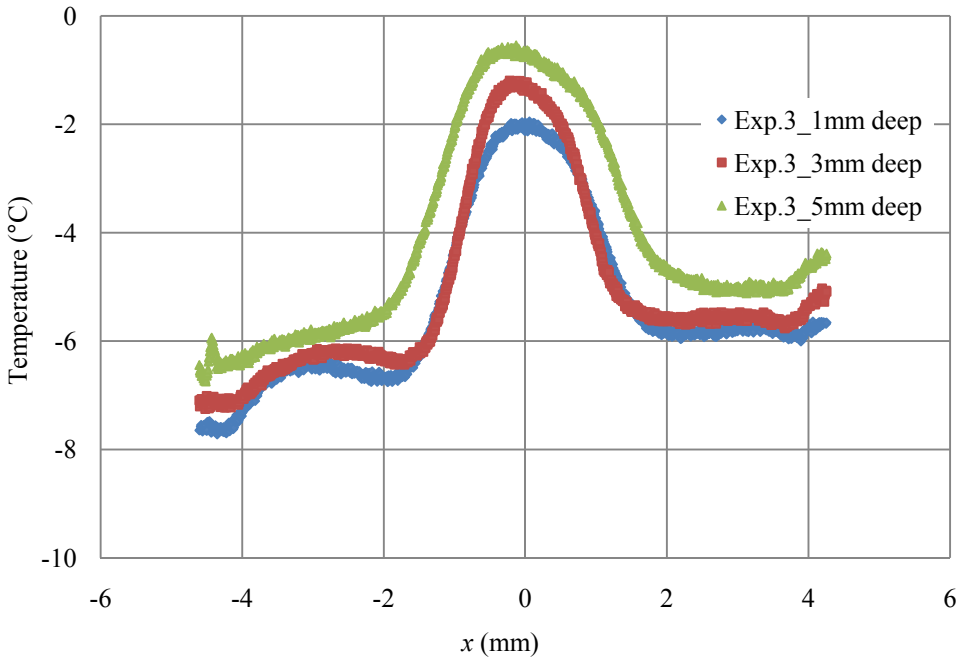

Figure 5-12. Horizontal temperature profile at a depth of 1 mm, 3 mm and 5 mm in the bulk water in experiment 3

5.4.2 Main source of error

In this PLIF measurement, a main error was induced in the temperature calibration step. This is because the temperature results used for temperature calibration obtained from the thermocouple measurement were coarse due to the large size of the thermocouple. As a result, any error in the thermocouple measurement would be applied to all the temperature maps. In addition, non-uniformity of the laser sheet could also induce error. Although theoretically, the two-color/two-dye PLIF measurement is independent of the laser intensity, any slight disagreement in overlapping the images from the two camera views may lead to significant error. However, these experimental errors will not change the temperature distribution pattern and trend. Therefore, conclusions about the relationship of temperature to the mechanisms driving the flow can be made.

5.5 Discussion and conclusion

In the stereo-PIV measurement that was described in Chapter 4, a convection pattern was observed and characterized at different vapor-phase pressures, including 430 Pa. The convection was found to be repeatable in different experiments that have the same experiment conditions. Since the PLIF measurements were implemented at the same experimental condition, it would be reasonable to expect the same convection to arise in the bulk water.

As introduced in Chapter 4, the evaporative flow was rotating around two centers that were symmetric to the centerline. The rotating process could mix the water in the side regions, causing the temperature distribution in these regions to become uniform. In contrast, the flow in the middle region moved upwards till it reached the water-vapor

interface, where the temperature is lower due to the evaporation cooling effect. Thus, the temperature distribution in this region should be decreasing with height due to thermal conduction. These inferences drawn from the results of the stereo-PIV investigation are confirmed by the temperature maps obtained from the PLIF investigation that was described above.

As can be seen in Fig. 5-4, the temperature on the centerline of the cuvette decreased linearly from ~-0.3°C, at the bottom of the cuvette, to ~-1.8°C, at 1 mm beneath the water-vapor interface. From there to the interface, the temperature was not shown in Fig. 5-4 because the fluorescence intensity ratio fluctuates dramatically. However, it can be seen in Fig. 5-7, Fig. 5-9 and Fig. 5-11 that the temperature in this region was still decreasing when approaching the water-vapor interface. According to the measured temperature profile in the middle region of the temperature map, and the relation between water density and temperature that was introduced in Chapter 1, it can be concluded that the column of the water in the middle region was density stabilized. In other words, there was no buoyancy driven flow in this region. Similarly, in the two side regions, there should not be any buoyancy driven convection either. This is because the water density was either decreasing with height, in Fig. 5-8 and Fig. 5-10, or nearly constant vertically with fluctuation.

In conclusion, as the existence of buoyancy driven flow was excluded, the observed evaporative convection can be attributed to surface tension driven only.

CHAPTER 6 : CONCLUSION

6.1 Summary of results

The study of Marangoni convection has been well developed for many liquids other than water [1]. Marangoni convection is usually weak and hence can hardly be observed in typical experiments. However, recent studies [1, 13-15] showed that when water evaporate at high rates, the surface tension gradients along the water-vapor interface, causing by the interfacial temperature variation induced by evaporation, can lead to Marangoni convection. Motivated by these studies, an experimental study has been performed to investigate the evaporative convection of water.

In this study, evaporative convection of water beneath a meniscus formed in a rectangular cuvette of 4mm×10mm in cross-section was investigated. A vacuum chamber system was designed to enable water to evaporate at different high steady evaporation rates. A temperature controlling system was also utilized to ensure that no buoyancy driven flow would be generated. The velocity field of the observed convection roll was visualized and characterized with application of the stereo-PIV. Its dependence on the evaporation rate, which was controlled by adjusting the vapor-phase pressure within the vacuum chamber, was experimentally examined. Along with the stereo-PIV investigation, a temperature measurement was implemented on the centerline of the cuvette using a thermocouple probe. The results indicated that the water was density stabilized on the

centerline of the cuvette. The Marangoni number was also estimated and found to be greater than the critical value, 80, for onset of Marangoni convection. It was also found to be inversely proportional to the vapor-phase pressure within the vacuum chamber.

In addition, the temperature profile of the observed convection field when the vapor-phase pressure was ~430 Pa was investigated by PLIF. The obtained temperature maps were found to be consistent with the results of the stereo-PIV investigation and the thermocouple measurement. The water density distribution in the convection field can also be determined since it is a function of temperature. According to the obtained temperature maps, it can be concluded that there was no buoyancy driven motion during the evaporation process of the water.

In conclusion, when the vapor-phase pressure was at ~430 Pa, the experimental results gathered in this thesis demonstrated that the observed evaporative convection of water was not driven by buoyancy forces, which indicates that surface tension driven flow was the most likely mechanism.

6.2 Future work

For future study on this phenomenon, some improvements on the experiment apparatus are strongly recommended. Firstly, a water supply system should be connected to the cuvette from its bottom to maintain the water surface at a constant level while evaporating. In this way, the evaporative convection will be more stabilized and observable spatially and temporally. In order to observe the convection from different viewing angles, a cuvette with a different cross-section, such as square, should be utilized. Secondly, a smaller thermocouple is necessary to enhance the accuracy of the

temperature measurement. Lastly, a smoother laser sheet will decrease errors significantly in the PLIF investigation.

REFERENCES

[1] K. Sefiane, and C. A. Ward, "Recent advances on thermocapillary flows and interfacial conditions during the evaporation of liquids", Adv. Colloid Interface Sci., Vol. 134-135, pp 201-223, 2007.

[2] Y. A. Cengel, R. H. Turner, and J. M. Cimbala, Fundamentals of thermal-fluid sciences, 3nd Ed., Boston: McGraw-Hill, 2001

[3] F. Duan, "Thermocapillary convection during evaporation", Ph.D. Thesis, University of Toronto, 2005

[4] X. Xu, and J. Luo, "Marangoni flow in an evaporating water droplet", Appl. Phys. Lett., vol. 91, pp. 124102, 2007.

[5] C. G. M. Marangoni, "Spreading of droplets of a liquid on the surface of another", Ann. Phys. Chem. Poggendorff, vol. 143, pp. 337-354, 1871.

[6] J. Tomson, "On certain curious motions observable at the surface of wine and other alcoholic liquors", Philos. Mag., Vol. 10, pp. 330-333, 1885.

[7] J. Tomson, "On a changing tessellated structure in certain liquids", Procs. Royal Phil. Soc. Glassgow, vol. 13, pp. 464-468, 1882.

[8] H. Bénard, "Les tourbillions cellulaires dans une nappe liquid", Rev. Gén. Sci. Pures Appl. vol. 11, pp. 1261-1271 and 130-1328, 1900.

[9] H. Bénard, “Les tourbillons cellulaires dans une nappe liquide transporatant de la chaleur par convection en régime permanent”, Ann. Chem. Phys., vol 23, pp. 62-144, 1901.

[10] J. R. A. Pearson, “On convection cells induced by surface tension”, J. Fluid Mech., vol. 4, pp. 489-500, 1958.

[11] E. L. Koschmieder, “Benard cell and Taylor vortices”, Cambridge: University Press, 1993.

[12] M. F. Schatz, S. J. VanHook, W. D. McCormick, J. B. Swift, and H. L. Swinney, “Onset of surface-tension-driven Benard convection”, Phys. Rev. Lett., vol. 75, pp. 1938-1941, 1995.

[13] C. A. Ward, and F. Duan. “Turbulent transition of thermocapillary flow induced by water evaporation”, Phys. Rev. E, vol. 69, pp. 056308, 2004.

[14] F. Duan, and C. A. Ward. “Surface excess properties from energy transport measurements during water evaporation”, Phys. Rev. E, vol. 72, pp. 056302, 2005.

[15] F. Duan, V. K. Badam, F. Durst, and C. A. Ward. “Thermocapillary transport of energy during water evaporation”, Phys. Rev. E, vol. 72, pp. 056303, 2005.

[16] C. Buffone , and K. Sefiane, “Investigation of thermocapillary convective patterns and their role in the enhancement of evaporation from pores”, Int. J. Multiphase Flow, vol. 30(9), pp. 1071-1091, 2004.

[17] C. Buffone , K. Sefiane, and J. R. E. Christy, “Experimental investigation of self-induced thermocapillary convection for an evaporating meniscus in capillary tubes using micro–particle image velocimetry”, Phys. Fluids, vol. 17, pp. 052104, 2005.

[18] C. Buffone, and K. Sefiane, “Controlling evaporative thermocapillary convection using external heating: An experimental investigation”, Exp. Therm. Fluid Sci., vol. 32, pp. 1287-1300, 2008.

[19] G. T. Barnes, A. I. Fehler “The measurement of temperature gradients in water during evaporation through monolayer-free and monolayer-covered surfaces”, J. Colloid Interface Sci. vol. 75, pp. 584-589, 1980.

[20] G. T. Barnes, D. S. Hunter, “Heat conduction during the measurement of the evaporation resistances of monolayers”, J. Colloid Interface Sci., vol. 88, pp. 437-443, 1981.

[21] D. Schreiber, H. K. Cammenga. "Conductive and convective heat transfer below evaporating liquid surfaces”, Ber. Bunsenges. Phys. Chem., vol. 85, pp. 909-914, 1981.

[22] H. K. Cammenga, D. Schrieber, and B. –E. Rudolph. "Two methods for measuring the surface temperature of evaporating liquids and results obtained with water”, J. Colloid Interface Sci. vol. 92, pp. 181-188, 1983.

[23] H. K. Cammenga, D. Schrieber, G. T. Barnes, and D. S. Hunter, “ On Marangoni convection during the evaporation of water”, J. Colloid Interface Sci., vol. 98, pp. 585-586, 1984.

[24] C. Hohmann, P. C. Stephan, “Microscale temperature measurement at an evaporating liquid meniscus”, Exp. Therm. Fluid Sci., vol. 26, pp. 157-162, 2002.

[25] F. Chauvet, S. Cazin, P. Duru, M, Prat, “Use of infrared thermography for the study of evaporation in a square capillary tube”, Int. J. Heat Mass Transfer, in press.

[26] R. J. Adrian, “Twenty years of particle image velocimetry”, Exp. Fluids, vol. 39, pp. 159–169, 2005.

[27] R. J. Adrian, “Scattering particle characteristics and their effect on pulsed laser measurements of fluid flow: speckle velocimetry vs. particle image velocimetry”, Appl. Opt., vol. 23, pp. 1690-1691, 1984.

[28] C. J. D. Pickering, N. Halliwell, “LSP and PIV: photographic film noise”, Appl. Opt., vol. 23, pp. 2961−2969, 1984.

[29] C. E. Willert, M. Gharib, “Digital particle image velocimetry”, Exp. Fluids, vol. 10, pp. 181-193, 1991.

[30] C. E. Willert, “Stereoscopic digital particle image velocimetry for application in wind tunnel flows”, Meas. Sci. Technol, Vol. 8, pp. 1465-1479, 1997.

[31] A. K. Prasad, R. J. Adrian, “ Investigation of non-penetrative thermal convection using stereoscopic particle image velocimetry”, SPIE, vol. 2005, pp. 667-682, 2005.

[32] J. Sakakibara, R. J. Adrian, “Whole field measurements of temperature in water using two-color laser induced fluorescence”, Exp. Fluids, vol. 26, pp.7–15, 1999.

[33] M. C. J. Coolen, R. N. Kieft, C. C. M. Rindt and A. A. van Steenhoven, “Application of 2-D LIF temperature measurements in water using a Nd:YAG laser”. Exp. Fluids, vol. 27, pp. 420–426, 1999.

[34] K. Hishida, J. Sakakibara, “Combined planar laser-induced fluorescence-particle image velocimetry technique for velocity and temperature fields”. Exp. Fluids, vol. 29, pp. s129–s140, 2000.

[35] H. Kim, K. Kihm, J. Allen, “Examination of ratiometric laser induced fluorescence thermometry for microscale spatial measurement resolution”. Int. J. Heat Mass Transfer, vol. 46(21), pp. 3967–3974, 2003.

[36] M. Bruchhausen, F. Guillard, F. Lemoine, “Instantaneous measurement of two-dimensional temperature distributions by means of two-color planar laser induced fluorescence (PLIF)”. Exp. Fluids, vol. 38, pp. 123-131, 2005.

[37] T. Nakajima, M. Utsunomiya, Y. Ikada, R. Matsumoto, “Simultaneous measurement of velocity and temperature of water using LDV and fluorescence techniqiue”. In: Proceedings of the 5th Symposium on Application of laser techniques to fluid mechanics, Lisbon. Instituto Superior Te´cnico, Lisbon, pp 2.6.1–2.6.6, 1990.

[38] J. Sakakibara, K. Hishida, M. Maeda, “Measurements of thermally stratified pipe flow using image processing techniques”. Exp. Fluids, vol. 16, pp.82–96, 1993.

[39] J. Sakakibara, K. Hishida, M. Maeda, “Vortex structure and heat transfer in the stagnation region of an impinging plane jet (simultaneous measurements of velocity and temperature fields by digital article image velocimetry and laser-induced fluorescence)”. Int. J. Heat Mass Transfer, vol. 40, pp.3163-3176, 1997.

[40] F. Lemoine, Y. Antoine, M. Wolff, M. Lebouche, “Simultaneous temperature and 2D velocity measurements in a turbulent heated jet using combined laser-induced fluorescence and LDA”. Exp. Fluids, vol. 26, pp. 315–323, 1999.

[41] Lo´pez Arbeloa I; Ruiz Ojeda P (1981) Molecular forms of rhodamine B. Chem Phys Lett 79: 347-350

[42] O. Auban, F. Lemoine, P. Vallette, J. Fontaine, “Simulation by solutal convection of a thermal plume in a confined stratified environment: application to displacement ventilation”. Int. J. Heat Mass Transfer, vol. 44, pp. 4679–4691, 2001.

[43] P. Lavieille, F. Lemoine, G. Lavergne, M. Lebouche´, “Evaporating and combusting droplet temperature measurements using two color laser-induced fluorescence”. Exp. Fluids, vol. 31, pp. 45–55, 2001.

[44] P. Lavieille, F. Lemoine, M. Lebouche´, “Investigation on temperature of evaporating droplets in linear stream using two-color laser-induced fluorescence”. Combust. Sci. Tech., vol. 174, pp. 117–142, 2002.

[45] P. Lavieille, A. Delconte, D. Blondel, M. Lebouche´, F. Lemoine, “Non-intrusive temperature measurements using three-color laserinduced fluorescence”. Exp. Fluids, vol. 36(5), pp. 706–716, 2004.

[46] A. E. Siegman, “Defining, measuring, and optimizing laser beam quality”, Proc. SPIE, vol. 1868, pp. 2-12, 1993

APPENDIX: DRAWINGS OF THE DESIGNED VACUUM SYSTEM

As illustrated in Fig. 2-4, the vacuum chamber is sealed by a Teflon flange and a copper block from its bottom. The copper block consists of two parts. In order to reduce thermal conduction between the copper block and the surroundings, a second Teflon gasket is utilized to avoid contact between screws and the copper block. Besides, the screw holes on the upper part of the copper block are slightly larger than the screws for the same reason. The thermoelectric cooling device is in contact with the bottom surface of the copper block. The drawings of these components are as follows.

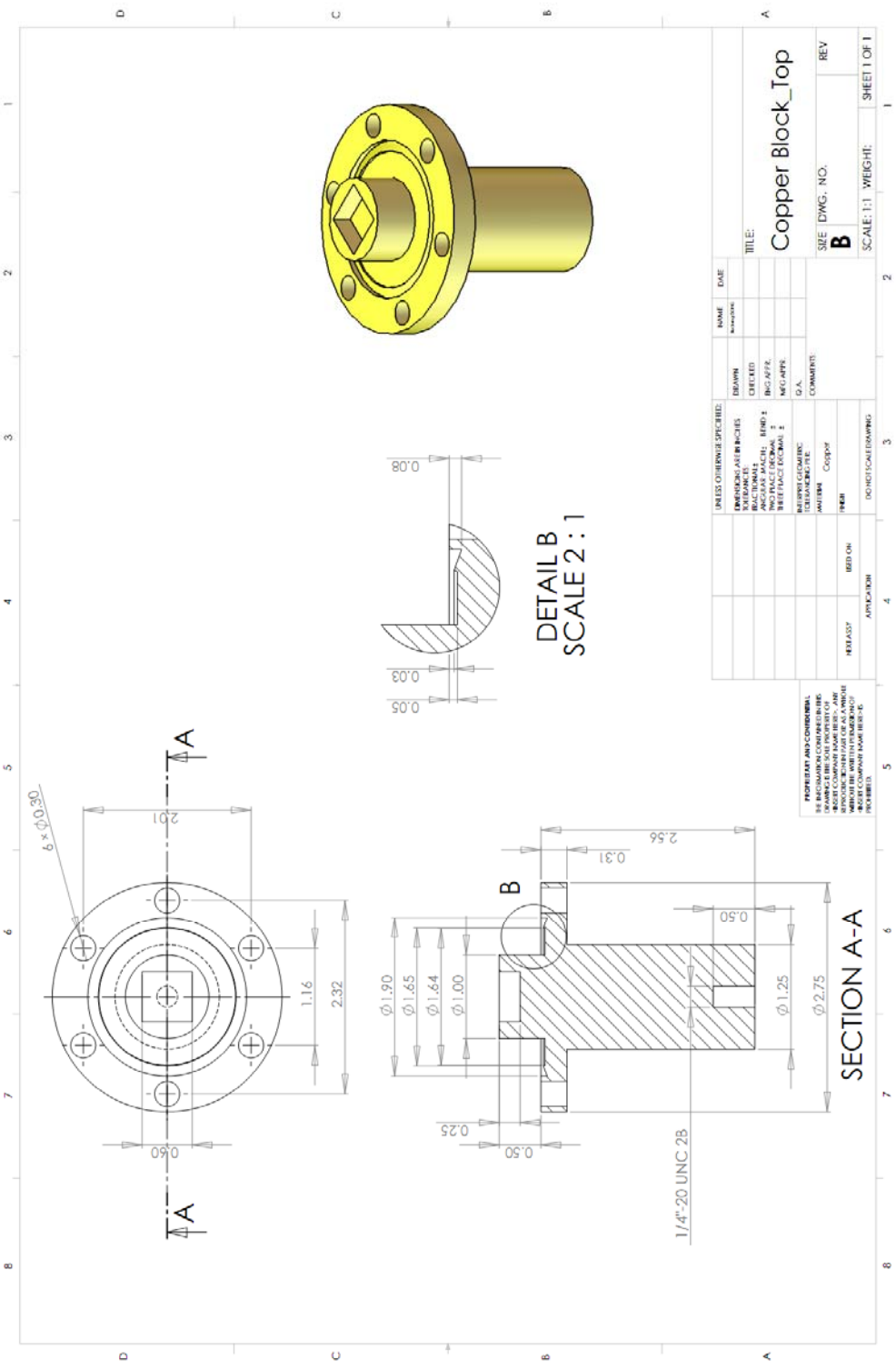

Figure A-1. Drawing of the upper part of the copper block

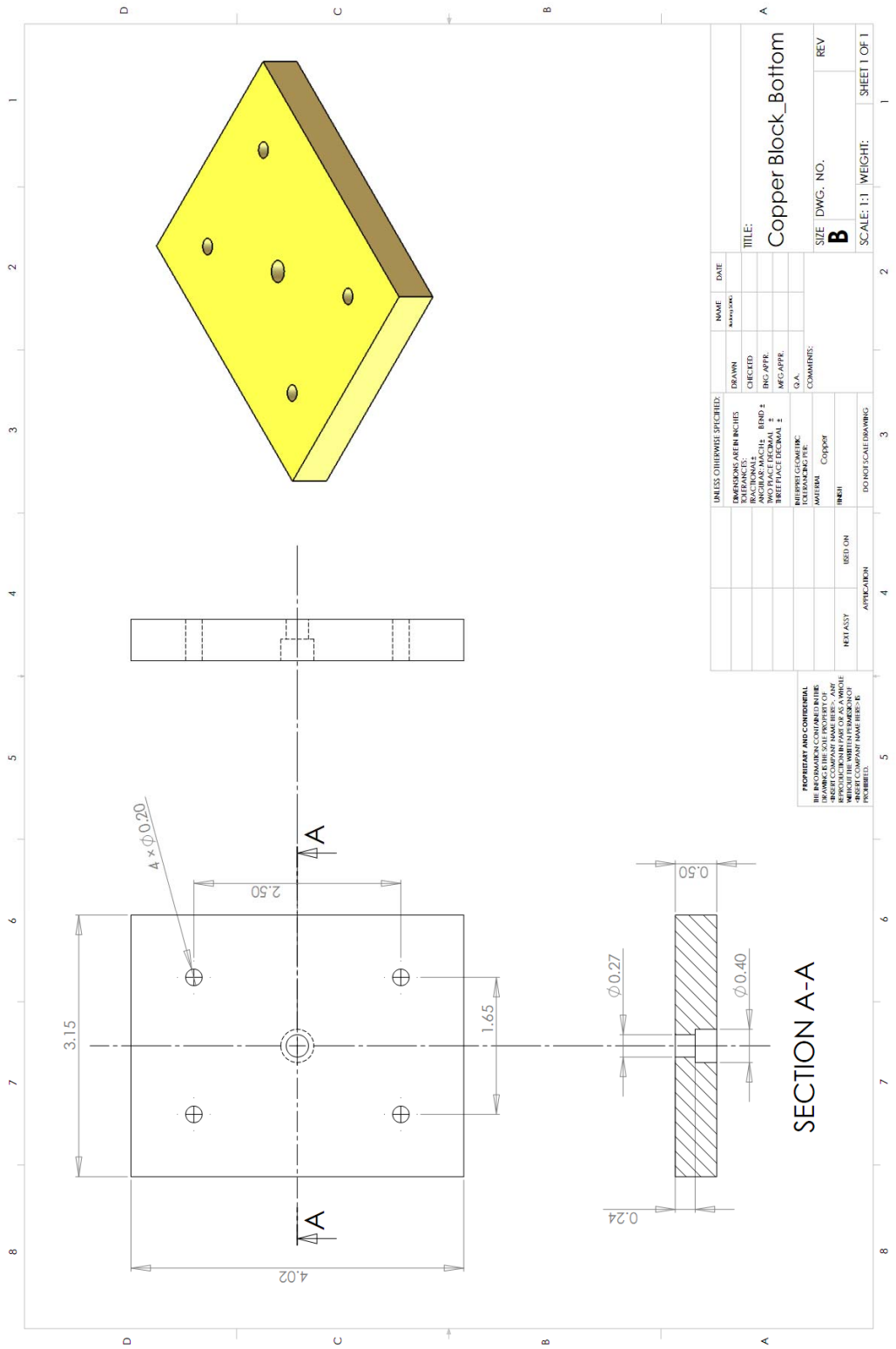

Figure A-2. Drawing of the bottom part of the copper block

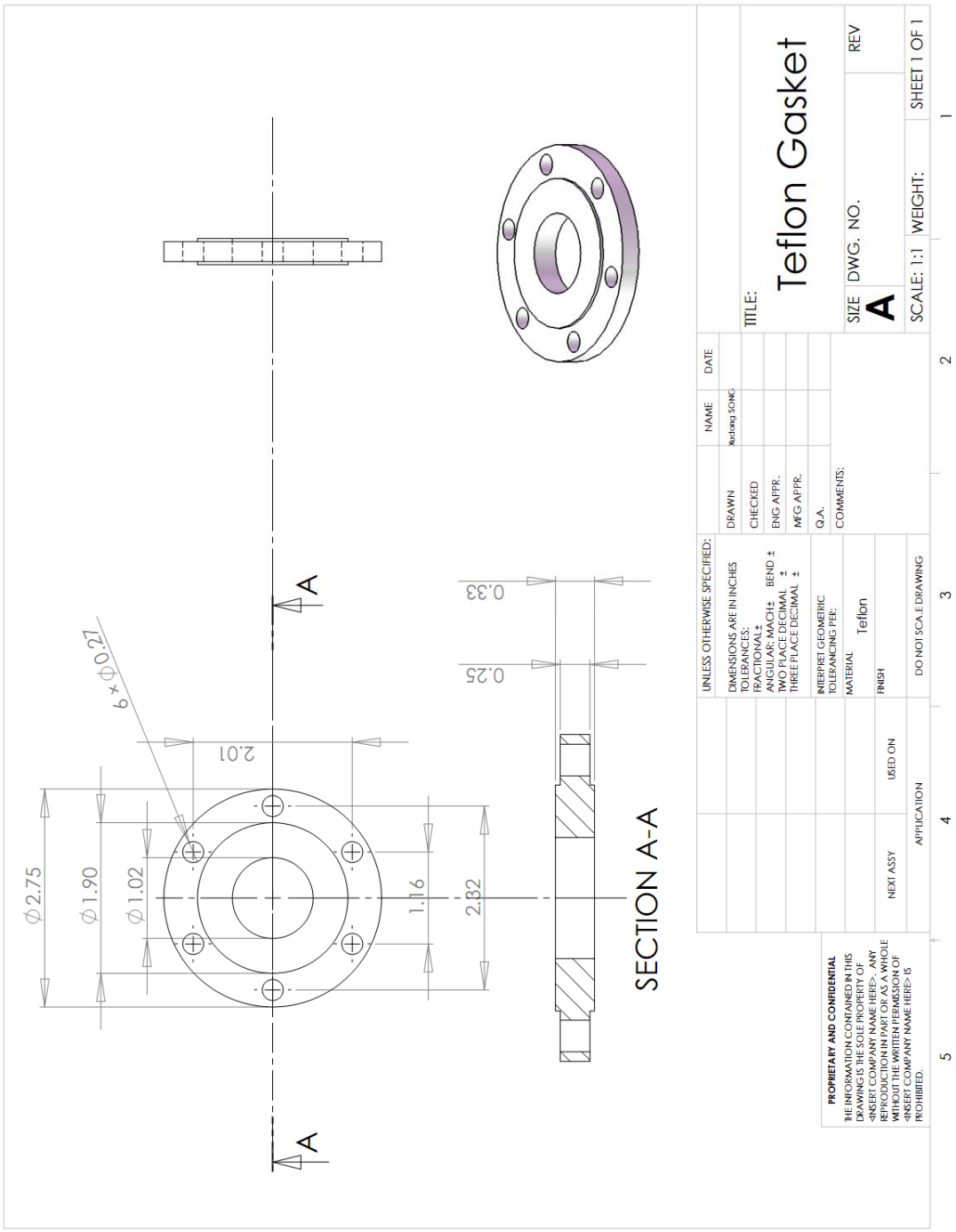

Figure A-3. Drawing of the Teflon gasket

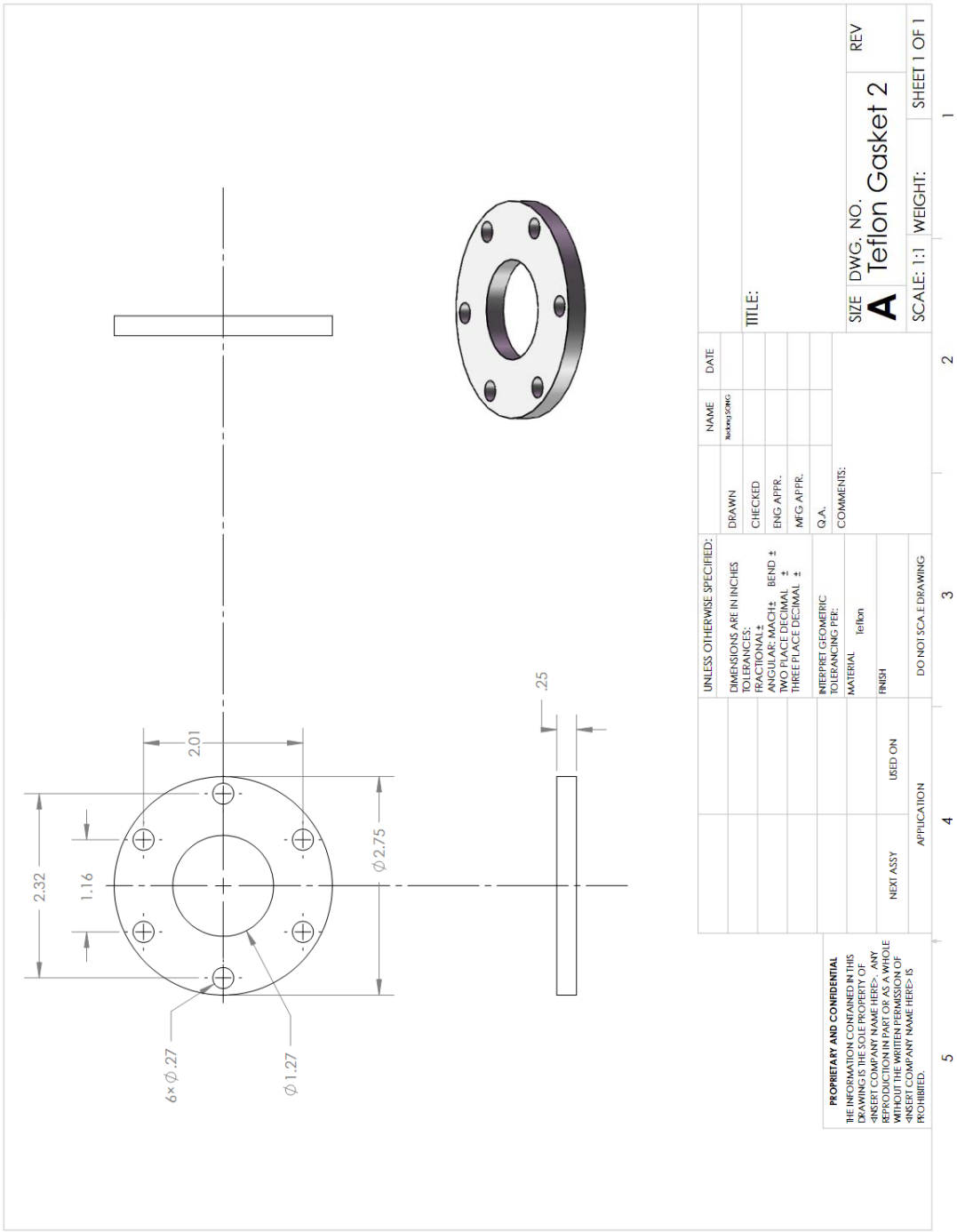

Figure A-4. Drawing of the Teflon gasket 2

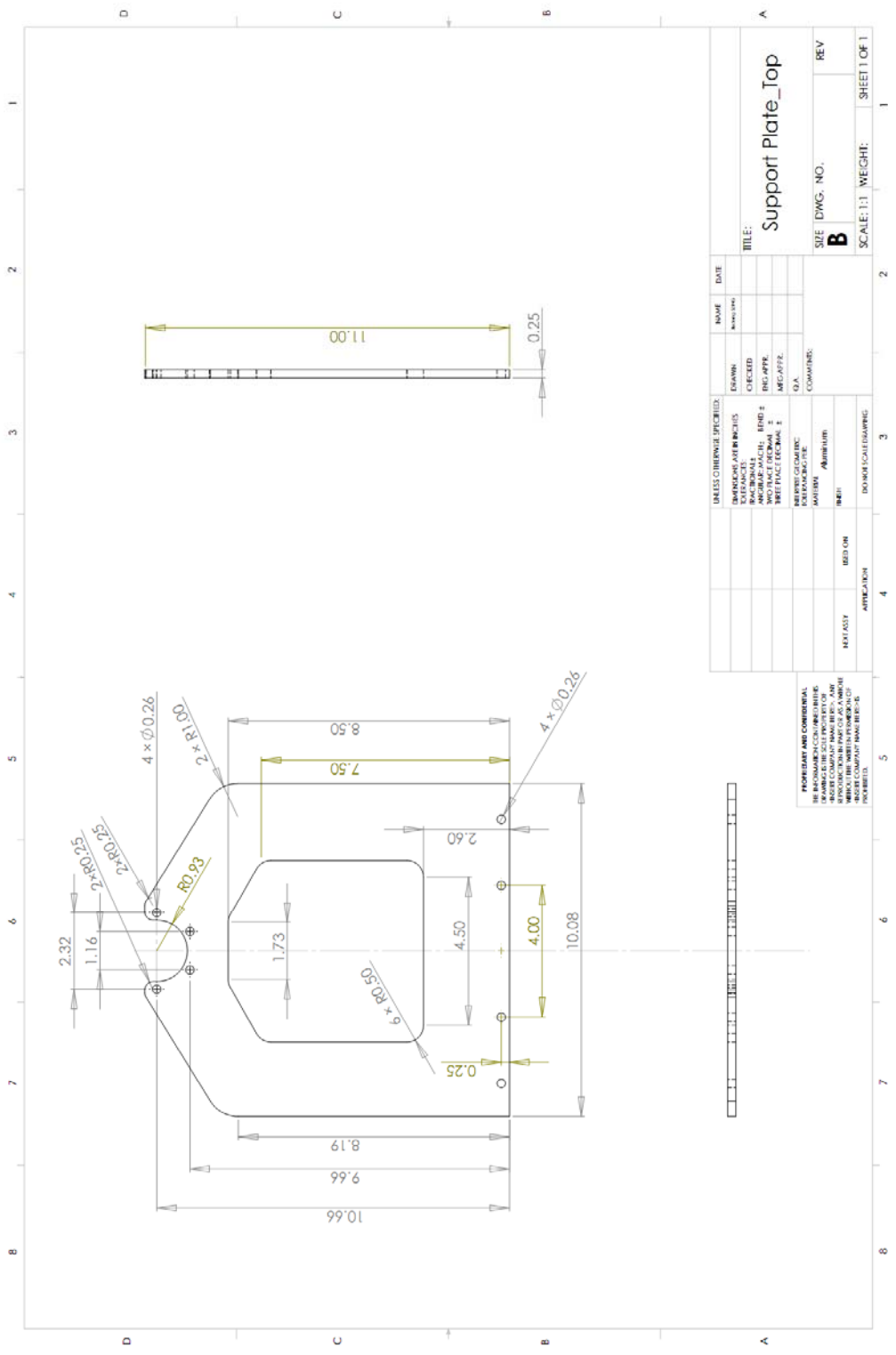

Figure A-5. Drawing of the upper part of the support plate

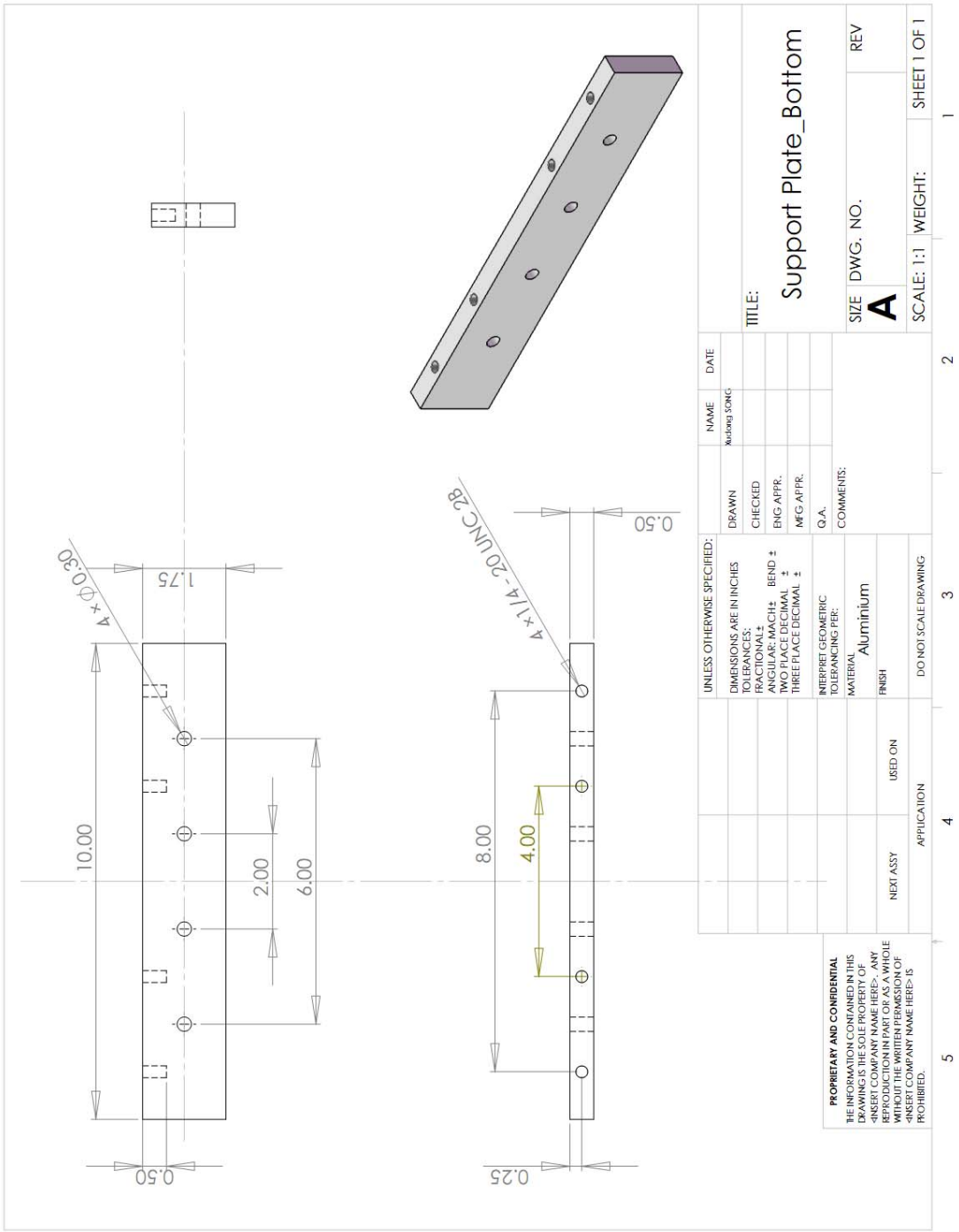

Figure A-6. Drawing of the bottom part of the support plate